TOI-1431b/MASCARA-5b: a highly irradiated ultrahot Jupiter orbiting one of the hottest and brightest known exoplanet host stars

Addison, B.C.; Knudstrup, E.; Wong, I.; Hébrard, G.; Dorval, P.; Snellen, I.; ... ; McLean, B.

Draft version November 7, 2021
Typeset using LaTeX twocolumn style in AASTeX63

TOI-1431 b/MASCARA-5 b: A Highly Irradiated Ultra-Hot Jupiter Orbiting One of the Hottest & Brightest Known Exoplanet Host Stars

Brett C. Addison,[1] Emil Knudstrup,[2] Ian Wong,[3,4] Guillaume Hébrard,[5] Patrick Dorval,[6] Ignas Snellen,[6] Simon Albrecht,[2] Aaron Bello-Arufe,[7] Jose-Manuel Almenara,[8] Isabelle Boisse,[9] Xavier Bonfils,[8] Shweta Dalal,[5] Olivier D. S. Demangeon,[10,11,12] Sergio Hoyer,[9] Flavien Kiefer,[13] N. C. Santos,[10,12] Grzegorz Nowak,[14,15] Rafael Luque,[14,15] Monika Stangret,[14,15] Enric Palle,[14,15] René Tronsgaard,[7] Victoria Antoci,[7] Lars A. Buchhave,[7] Maximilian N. Günther,[16,17] Tansu Daylan,[16,18] Felipe Murgas,[14,15] Hannu Parviainen,[14,15] Emma Esparza-Borges,[14,15] Nicolas Crouzet,[19] Norio Narita,[20,21,22,23] Akihiko Fukui,[24,14] Kiyoe Kawauchi,[24] Noriharu Watanabe,[25,26,22] Markus Rabus,[27,28,29] Marshall C. Johnson,[28] Gilles P. P. L. Otten,[30,9] Geert Jan Talens,[31] Samuel H. C. Cabot,[32] Debra A. Fischer,[32] Frank Grundahl,[2] Mads Fredslund Andersen,[2] Jens Jessen-Hansen,[2] Pere Pallé,[14,15] Avi Shporer,[16] David R. Ciardi,[33] Jake T. Clark,[1] Robert A. Wittenmyer,[1] Duncan J. Wright,[1] Jonathan Horner,[1] Karen A. Collins,[34] Eric L. N. Jensen,[35] John F. Kielkopf,[36] Richard P. Schwarz,[37] Gregor Srdoc,[38] Mesut Yilmaz,[39] Hakan Volkan Senavci,[39] Brendan Diamond,[40] Daniel Harbeck,[28] Thaddeus D. Komacek,[41] Jeffrey C. Smith,[42,43] Songhu Wang,[44] Jason D. Eastman,[45] Keivan G. Stassun,[46,47] David W. Latham,[45] Roland Vanderspek,[48] Sara Seager,[48,49,50] Joshua N. Winn,[51] Jon M. Jenkins,[42] Dana R. Louie,[52] Luke G. Bouma,[53] Joseph D. Twicken,[42,43] Alan M. Levine,[16] and Brian McLean[54]

[1] University of Southern Queensland, Centre for Astrophysics, USQ Toowoomba, West Street, QLD 4350 Australia
[2] Stellar Astrophysics Centre, Department of Physics and Astronomy, Aarhus University, Ny Munkegade 120, DK-8000 Aarhus C, Denmark
[3] Department of Earth, Atmospheric, and Planetary Sciences, Massachusetts Institute of Technology, Cambridge, MA 02139, USA
[4] 51 Pegasi b Fellow
[5] Institut dAstrophysique de Paris, UMR7095 CNRS, Universite Pierre & Marie Curie, 98bis boulevard Arago, 75014 Paris, France
[6] Leiden Observatory, Leiden University, Postbus 9513, 2300 RA Leiden, NL
[7] DTU Space, National Space Institute, Technical University of Denmark, Elektrovej 328, DK-2800 Kgs. Lyngby, Denmark
[8] Université Grenoble Alpes, CNRS, IPAG, 38000 Grenoble, France
[9] Aix Marseille Univ, CNRS, CNES, LAM, Marseille, France
[10] Instituto de Astrofísica e Ciências do Espaço, Universidade do Porto, CAUP, Rua das Estrelas, 4150-762 Porto, Portugal
[11] Centro de Astrofísica da Universidade do Porto, Rua das Estrelas, 4150-762 Porto, Portugal
[12] Departamento de Física e Astronomia, Faculdade de Ciências, Universidade do Porto, Rua Campo Alegre, 4169-007, Porto, Portugal
[13] LESIA, Observatoire de Paris, Université PSL, CNRS, Sorbonne Université, Université de Paris, 5 place Jules Janssen, 92195 Meudon, France
[14] Instituto de Astrofísica de Canarias (IAC), E-38200 La Laguna, Tenerife, Spain
[15] Dept. Astrofísica, Universidad de La Laguna (ULL), E-38206 La Laguna, Tenerife, Spain
[16] Department of Physics and Kavli Institute for Astrophysics and Space Research, Massachusetts Institute of Technology, Cambridge, MA 02139, USA
[17] Juan Carlos Torres Fellow
[18] Kavli Fellow
[19] European Space Agency (ESA), European Space Research and Technology Centre (ESTEC), Keplerlaan 1, 2201 AZ Noordwijk, The Netherlands
[20] Komaba Institute for Science, The University of Tokyo, 3-8-1 Komaba, Meguro, Tokyo 153-8902, Japan
[21] JST, PRESTO, 3-8-1 Komaba, Meguro, Tokyo 153-8902, Japan
[22] Astrobiology Center, 2-21-1 Osawa, Mitaka, Tokyo 181-8588, Japan
[23] Instituto de Astrofísica de Canarias (IAC), 38205 La Laguna, Tenerife, Spain
[24] Department of Earth and Planetary Science, The University of Tokyo, Tokyo, Japan

Corresponding author: Brett C. Addison
Brett.Addison@usq.edu.au

[25]Department of Astronomical Science, The Graduate University for Advanced Studies, SOKENDAI, 2-21-1 Osawa, Mitaka, Tokyo 181-8588, Japan
[26]National Astronomical Observatory of Japan, NINS, 2-21-1 Osawa, Mitaka, Tokyo 181-8588, Japan
[27]Departamento de Matemática y Fı'sica Aplicadas, Universidad Católica de la Santísima Concepción, Alonso de Rivera 2850, Concepción, Chile
[28]Las Cumbres Observatory, 6740 Cortona Dr., Ste. 102, Goleta, CA 93117, USA
[29]Department of Physics, University of California, Santa Barbara, CA 93106-9530, USA
[30]Academia Sinica, Institute of Astronomy and Astrophysics, 11F Astronomy-Mathematics Building, NTU/AS campus, No. 1, Section 4, Roosevelt Rd., Taipei 10617, Taiwan
[31]Institut de Recherche sur les Exoplanètes, Département de Physique, Université de Montréal, Montréal, QC H3C 3J7, Canada
[32]Department of Astronomy, Yale University, 52 Hillhouse Ave, New Haven, CT 06511, USA
[33]NASA Exoplanet Science Institute, Caltech/IPAC, 1200 East California Avenue, Pasadena, CA 91125
[34]Center for Astrophysics | Harvard & Smithsonian, 60 Garden Street, Cambridge, MA 02138, USA
[35]Department of Physics & Astronomy, Swarthmore College, Swarthmore PA 19081, USA
[36]Department of Physics and Astronomy, University of Louisville, Louisville, KY 40292, USA
[37]Patashnick Voorheesville Observatory, Voorheesville, NY 12186, USA
[38]Kotizarovci Observatory, Sarsoni 90, 51216 Viskovo, Croatia
[39]Ankara University, Department of Astronomy and Space Sciences, TR-06100, Ankara, Turkey
[40]Howard Community College, 10901 Little Patuxent Pkwy, Columbia, MD 21044, USA
[41]Department of the Geophysical Sciences, The University of Chicago, Chicago, IL, 60637, USA
[42]NASA Ames Research Center, Moffett Field, CA 94035, USA
[43]SETI Institute, 189 Bernardo Ave., Suite 200, Mountain View, CA 94043, USA
[44]Astronomy Department, Indiana University Bloomington, 727 East 3rd Street, Swain West 318, IN 4740, USA
[45]Center for Astrophysics | Harvard & Smithsonian, 60 Garden Street, Cambridge, MA 02138, USA
[46]Department of Physics and Astronomy, Vanderbilt University, Nashville, TN 37235, USA
[47]Department of Physics, Fisk University, Nashville, TN 37208, USA
[48]MIT Kavli Institute for Astrophysics and Space Research, Massachusetts Institute of Technology, Cambridge, MA 02139, USA
[49]Earth and Planetary Science, Massachusetts Institute of Technology, 77 Massachusetts Avenue, Cambridge, MA 02139, USA
[50]Department of Aeronautics and Astronautics, Massachusetts Institute of Technology, 77 Massachusetts Avenue, Cambridge, MA 02139, USA
[51]Department of Astrophysical Sciences, Princeton University, Peyton Hall, 4 Ivy Lane, Princeton, NJ 08544, USA
[52]University of Maryland, Department of Astronomy, College Park, MD 20742-2421, USA
[53]Department of Astrophysical Sciences, Princeton University, 4 Ivy Lane, Princeton, NJ 08544, USA
[54]Space Telescope Science Institute, 3700 San Martin Drive, Baltimore, MD, 21218, USA

Submitted to The Astronomical Journal

ABSTRACT

We present the discovery of a highly irradiated and moderately inflated ultra-hot Jupiter, TOI-1431 b/MASCARA-5 b (HD 201033 b), first detected by NASA's Transiting Exoplanet Survey Satellite mission (*TESS*) and the Multi-site All-Sky CAmeRA (MASCARA). The signal was established to be of planetary origin through radial velocity measurements obtained using SONG, SOPHIE, FIES, NRES, and EXPRES, which show a reflex motion of $K = 294.1 \pm 1.1$ m s^{-1}. A joint analysis of *TESS*, MuSCAT2, and LCOGT photometry, radial velocity measurements, and the spectral energy distribution of the host star reveals that TOI-1431 b has a mass of $M_p = 3.14^{+0.19}_{-0.18}\,\mathrm{M_J}$ ($1000 \pm 60\,\mathrm{M_\oplus}$), an inflated radius of $R_p = 1.51 \pm 0.06\,\mathrm{R_J}$ ($16.9^{+0.7}_{-0.6}\,\mathrm{R_\oplus}$), and an orbital period of $P = 2.65022 \pm 0.00001$ d. The planet orbits a bright (V = 8.049 mag) and young ($0.29^{+0.32}_{-0.19}$ Gyr) Am type star with $T_{\rm eff} = 7690^{+400}_{-250}$ K, resulting in a highly irradiated planet with an incident flux of $\langle F \rangle = 7.24^{+0.68}_{-0.64} \times 10^9$ erg s^{-1} cm^{-2} ($5300^{+500}_{-470}\mathrm{S_\oplus}$) and an equilibrium temperature of $T_{eq} = 2370 \pm 100$ K. *TESS* photometry also reveals a secondary eclipse with a depth of 124 ± 5 ppm as well as the full phase curve of the planet's thermal emission in the red-optical. This has allowed us to measure the dayside and nightside temperature of its atmosphere as $T_{\rm day} = 2983^{+63}_{-68}$ K and $T_{\rm night} = 2556^{+62}_{-65}$ K, the second hottest measured nightside temperature. The planet's low day/night temperature contrast (∼400 K) suggests very efficient heat transport between the dayside and nightside hemispheres. Given the host star brightness and estimated secondary eclipse depth of ~ 1000 ppm in the K-band, the secondary eclipse is potentially detectable at near-IR wavelengths with ground-based facilities, and the planet is ideal for intensive atmospheric characterization through transmission and emission spectroscopy from space missions such as with the James Webb Space Telescope and the Atmospheric Remote-sensing Infrared Exoplanet Large-survey.

Keywords: stars: individual (HD 201033) — techniques: radial velocities – techniques: transits

1. INTRODUCTION

Exoplanet discoveries over the past 25 years have revealed that the diversity of alien worlds to be far greater than we had ever imagined. Planets more massive than Jupiter were found on orbits measured in mere days (and became known as "hot Jupiters", e.g. Butler et al. 1998; Henry et al. 2000; Tinney et al. 2001a), while others were found moving on highly eccentric orbits that had more in common with the Solar System's cometary bodies than its planets (e.g. Naef et al. 2001; Jones et al. 2006; Wittenmyer et al. 2017, 2019; Bergmann et al. 2021). And more recently, a new class of close-in gas giants has emerged that are hotter than even the coolest main-sequence stars. These super hot gas giants are known as ultra-hot Jupiters and have dayside temperatures $\gtrsim 2200$ K (e.g., Parmentier et al. 2018).

In the early years of the Exoplanet era, the majority of new exoplanet discoveries were made by radial velocity surveys (e.g. Mayor & Queloz 1995; Cochran et al. 1997; Butler et al. 1999; Pepe et al. 2004; Endl et al. 2008; Vogt et al. 2010) that mainly targeted stars considered to be 'Sun-like': of spectral classes late-F, G, and K. The focus on such stars was, in part, driven by technical necessity — such stars possess ample spectral lines for radial velocity analysis and typically rotate slowly enough that such lines are sufficiently narrow enough to yield precise radial velocity measurements. As a result, during the first two decades of the Exoplanet era, our knowledge of the diversity of planets was heavily biased towards systems with host stars similar to the Sun.

The situation changed with the launch of the *Kepler* space observatory, designed to search for exoplanets using the transit technique (Borucki et al. 2010). By surveying a vast number of stars at once, *Kepler* was able to get a true handle on the frequency of short-period planets around a wide variety of stars. It showed that planets are ubiquitous — a natural byproduct of the star formation process — and that planetary systems have a wide variety of architectures and compositions (e.g. Rogers 2015; Guenther et al. 2017; Dorn et al. 2019; Hsu et al. 2019; Cañas et al. 2019; Millholland et al. 2016, 2017; Bryson et al. 2021).

Although the transit technique is better suited to find planets around hot, massive stars than the radial velocity method (Zhou et al. 2016b; Lund et al. 2017; Siverd et al. 2018a; Martínez et al. 2020; Newton et al. 2019), such discoveries remain challenging due to the inherent difficulty in confirming planet candidates with radial velocity measurements. This is because more massive stars tend to have rapid rotation, resulting in a significant decrease in the obtainable radial velocity precision.

NASA's *Transiting Exoplanet Survey Satellite* (*TESS*; Ricker et al. 2015) was launched in 2018 and is the successor to the hugely successful *Kepler* and K2 missions. While the *Kepler* spacecraft could only examine a $\sim 115°$ patch of sky ($\sim 0.3\%$ total area of the full sky) at any given time (performing a narrow but deep survey of the sky), *TESS* is designed to survey large bands of the sky at a time (96° by 24°). As a result, over the two years of *TESS*' primary mission, it surveyed the majority of the sky, obtaining high cadence observations (one target pixel image recorded every two minutes) of more than 200,000 pre-selected main-sequence dwarf stars, and low cadence observations (one full frame image every thirty minutes) of 20 million bright stars (Ricker et al. 2015). In doing so, it has enabled the search for planets around a wide variety of bright stars (including hot and more massive stars historically avoided in radial velocity surveys) — perfect targets for ground-based follow-up observations. While we are still in the early stages of reaping the full harvest from *TESS*' remarkable wealth of observations, the spacecraft has already led to the discovery of a number of fascinating new planets (e.g. Huang et al. 2018; Wang et al. 2019; Newton et al. 2019; Addison et al. 2020; Gilbert et al. 2020; Plavchan et al. 2020; Teske et al. 2020; Jones et al. 2019; Cañas et al. 2019; Günther et al. 2019; Jordán et al. 2020; Davis et al. 2020; Brahm et al. 2020).

A great benefit of *TESS*' discoveries orbiting bright stars is that those stars make ideal targets for follow-up observations, allowing us to better characterize the planets that orbit them. The most obvious route by which such characterization is achieved is through radial velocity observations, which provide measurements of the masses of the planets. Additionally, radial velocity observations also provide vital information on the planet's orbit, including its eccentricity and orbital period (critical if only one or two transits are observed). These observations can also be used to reveal the presence of otherwise undetectable, non-transiting planetary companions (e.g. Mills et al. 2019; Weiss et al. 2020; Sozzetti et al. 2021). When radial velocity observations are made during a transit of a planet across the disk of its host star, they can be used to constrain the inclination of the planet's orbit relative to the plane of the host star's equator through the use of the 'Rossiter-McLaughlin effect' (e.g., Rossiter 1924; McLaughlin 1924).

Such observations have yielded startling insights in recent years. Where predictions made based on our knowledge of the Solar System would suggest that exoplanets should, typically, move in roughly the same plane as their host star's equator, Rossiter-McLaughlin observations have revealed that a significant fraction of hot Jupiters move on misaligned orbits. Surprisingly, such observations have even revealed a number of planets moving on polar or retrograde orbits (e.g. Winn et al. 2009; Hirano et al. 2011; Albrecht et al. 2012; Addison et al. 2013) — a scenario markedly different from the near coplanarity of the Solar System (as discussed in Horner et al. 2020, and references therein).

The highly excited orbits of such inclined hot Jupiters are likely linked to their origins. A number of different mechanisms have been proposed to produce hot Jupiters, ranging from the smooth and relatively sedate inward migration of the giant planets through interactions with their host star's protoplanetary disk (e.g. Lin et al. 1996; Ward 1997; Tanaka et al. 2002; Alibert et al. 2005), to planet-planet scattering (where close encounters between two planets throw them both onto highly eccentric orbits, dropping one inwards, towards its host, and flinging the other outwards; see e.g., Chatterjee et al. 2008; Beaugé & Nesvorný 2012; Li et al. 2019a), and even distant perturbations from binary companions (through the Kozai-Lidov mechanism; see e.g. Kozai 1962; Lidov 1962; Nagasawa et al. 2008). Those mechanisms that invoke a period of high orbital eccentricity then require the tidal circularization of the planet's orbit, which, for small pericenter distances, can happen on timescales far shorter than the lifetimes of the stars involved (Nagasawa et al. 2008).

These three methods would naturally produce very different populations of hot Jupiters. Those formed through disk migration would be expected to orbit in essentially the same plane as their host star's equator. Those formed through planet-planet scattering would likely also congregate around such low inclinations, but would be more dispersed/excited, with scattering events able to produce at least moderate orbital inclinations for the planets involved. Planets that migrate as a result of the Kozai-Lidov mechanism, by contrast, would be expected to be found on highly misaligned orbits, as the Kozai-Lidov mechanism causes significant inclination excitation as a byproduct of the eccentricity excitation driving the planetary migration.

Given that more massive stars are statistically more likely to host binary companions (e.g. Perryman et al. 1998; Böhm-Vitense 2007; Zinnecker & Yorke 2007), especially Am stars such as TOI-1431 (see, Böhm-Vitense 2006), and also tend to form more massive planets (e.g. Ida & Lin 2005; Bowler et al. 2010; Reffert et al. 2015a), it would seem reasonable to expect that such stars might be more likely to host both moderately and highly misaligned planets (since the two mechanisms by which excited hot Jupiters can be produced would be more likely to occur). Indeed, as the catalog of planets for which spin-orbit alignment measurements have been made has grown, this prediction appears to have been borne out. The fraction of highly misaligned planets appears to be a strong function of stellar effective temperature (and to a lesser degree stellar mass), with hotter and more massive stars far more likely to host such planets than those that are cooler and less massive (e.g., Winn et al. 2010; Triaud et al. 2010; Louden et al. 2021).

In this work, we expand the catalog of planets orbiting hot main-sequence stars with the discovery and characterization of TOI-1431 b/MASCARA-5b — an inflated, ultra-hot Jupiter orbiting a massive, hot, and metal-peculiar Am star.

In Section 2, we describe the observations and data reduction. The host star properties derived from the analysis of the broadband spectral energy distribution and spectroscopy are outlined in Section 3. The data analysis, modeling, and results are presented in Section 4. We then discuss the phase curve and secondary eclipse analysis and measurements of the planet's dayside and nightside temperatures in Section 5. Lastly, the discussion and conclusions are provided in Sections 6 and 7, respectively.

2. OBSERVATIONS AND DATA REDUCTION

TOI-1431/MASCARA-5 (HD 201033) was observed with space-based photometry by *TESS* (Section 2.1) and ground-based photometry from several facilities (Section 2.2). We also obtained follow-up spectroscopic observations from several ground-based facilities (Section 2.3) as well as high-contrast imaging on the Keck II telescope (Section 2.4) to establish the planetary nature of the transit signals detected by *TESS* and the Multi-site All-Sky CAmeRA. Here we describe the observations collected and the data reduction process.

2.1. *TESS Photometry*

The star TOI-1431 (HD 201033; TIC 375506058, Stassun et al. 2019) was observed in Sectors 15 (on Camera 2 and CCD chip number 4) and 16 (on Camera 2 and CCD chip number 3) by *TESS* in 2-minute cadence mode nearly continuously between 2019 August

15 and 2019 October 7. The photometric data were processed by the *TESS* Science Processing Operations Center (SPOC) pipeline (see, Jenkins et al. 2016, for a description of the SPOC pipeline), resulting in two versions of the light curves: Simple Aperture Photometry (SAP, see, Twicken et al. 2010; Morris et al. 2020) and Presearch Data Conditioning (PDC, see, Stumpe et al. 2012, 2014; Smith et al. 2012). We downloaded both versions of the light curves from the NASA's Mikulski Archive for Space Telescopes (MAST).

The transiting planet candidate was promoted to *TESS* Object of Interest (TOI) status and designated TOI 1431.01 by the *TESS* Science Office based on model fit results and a passing grade on all diagnostic tests in the SPOC Data Validation (DV) report (Twicken et al. 2018; Li et al. 2019b) for Sector 15. Twenty transits (10 per sector), were observed by *TESS*. Each transit had a duration of ∼2.5 hr, a depth of ∼6000 parts per million (ppm), and recurred with a period of 2.65 d. The first detected transit occurred on $\mathrm{BJD_{TDB}}$ 2458712 in Sector 15. The raw SAP and PDC light curves are shown in Figure 1.

Before detrending and fitting the SAP and PDC light curves, we first removed all quality-flagged data. The light curves were then split into a total of 10 segments, with each segment split at the spacecraft momentum dumps[1] at 4.25 day and 5.83 day intervals in Sectors 15 and 16, respectively, to minimize the offset effects on the light curves during the detrending and fitting analysis. The transits were then masked and a 5σ median filter was applied to the out-of-transit data to remove remaining outliers in each light curve segment. Lastly, the light curve segments were normalized with the mean of the out-of-transit flux before performing the detrending and fitting analysis as described in Section 4.1.

2.2. *Ground-Based Transit Photometry*

Transit signals of TOI-1431 b were first detected by the ground-based Multi-site All-Sky CAmeRA (MASCARA) telescope (Talens et al. 2017) at the Roque de los Muchachos Observatory, La Palma, starting in February 2015. Transits were observed by MASCARA between February 2015 to March 2018 and were discovered before *TESS* observed them. Figure 2 shows the phase-folded light curve of TOI-1431 b from MASCARA with the transit signal clearly detected at the same ~ 2.65 d period and approximate transit depth as measured by *TESS*. The MASCARA observations were taken with exposure times of 6.4 s without using any filters and achieve a photometric precision of ~ 5000 ppm, per 5 m binned observation.

Both MASCARA and *TESS* have large on-sky pixel sizes of $1'\,\mathrm{pixel}^{-1}$ (Talens et al. 2017) and $0.35'\,\mathrm{pixel}^{-1}$ (Ricker et al. 2015), respectively. As such, further photometric follow-up is required to rule out potential false positive scenarios such as nearby eclipsing binaries, where an eclipsing binary pair falls on or very close to the same pixel as the target star in the MASCARA and *TESS* images.

To confirm the transit signals detected by *TESS* and MASCARA were coming from TOI-1431 and to check for any changes in transit depth between multiple photometric bands (chromaticity), we acquired additional photometric follow-up observations from several ground-based facilities through the *TESS* Follow-up Observing Program (TFOP) Working Group as summarized in Table 4 in the Appendix. We used the *TESS* Transit Finder which is a customized version of the Tapir software package (Jensen 2013), to schedule the observations. These facilities include the MuSCAT2 imager on the 1.52 m Carlos Sanchez Telescope (TCS) at the Teide Observatory (OT), the Las Cumbres Observatory Global Telescope (LCOGT; Brown et al. 2013a) 1-m node at the McDonald Observatory, the 0.3 m telescope at the Kotizarovci Observatory (SCT) in Rijeka, Croatia, the 0.36 m CDK14 telescope at Howard Community College, the 0.8 m telescope at the Ankara University Kreiken Observatory (AUKR), and the 0.6 m University of Louisville Manner Telescope (ULMT) at Mt. Lemmon. For the final global analysis with `Allesfitter`, we included only the high-quality and high-precision (RMS $\lesssim$ 1 ppt) ground-based observations with full transit coverage that are free of significant systematics to provide precise transit depth measurements and accurate transit ephemeris. As such, we only include the light curves from MuSCAT2 observed on 16 May 2020 and LCOGT taken on 14 October 2020.

2.2.1. *MuSCAT2*

Two full transits of TOI-1431 b were observed with MuSCAT2, one on 16 May 2020 and a second one on 24 May 2020, using simultaneous multi-color photometry in g', r', i', and z_s bands (Narita et al. 2019). For the global fitting, we only used the transit observed on 16 May 2020 since the second transit observation was affected by systematics due to weather, resulting in different transit depths between the filter bands and residuals larger than 1.0 ppt. On the night of 16 May 2020, de-focused observations were taken from 01:50 UT to 05:22 UT, with exposure times of 8 s for all channels, except for the r', where an exposure time of 5 s was used

[1] As provided in the data release notes found at https://archive.stsci.edu/tess/tess_drn.html

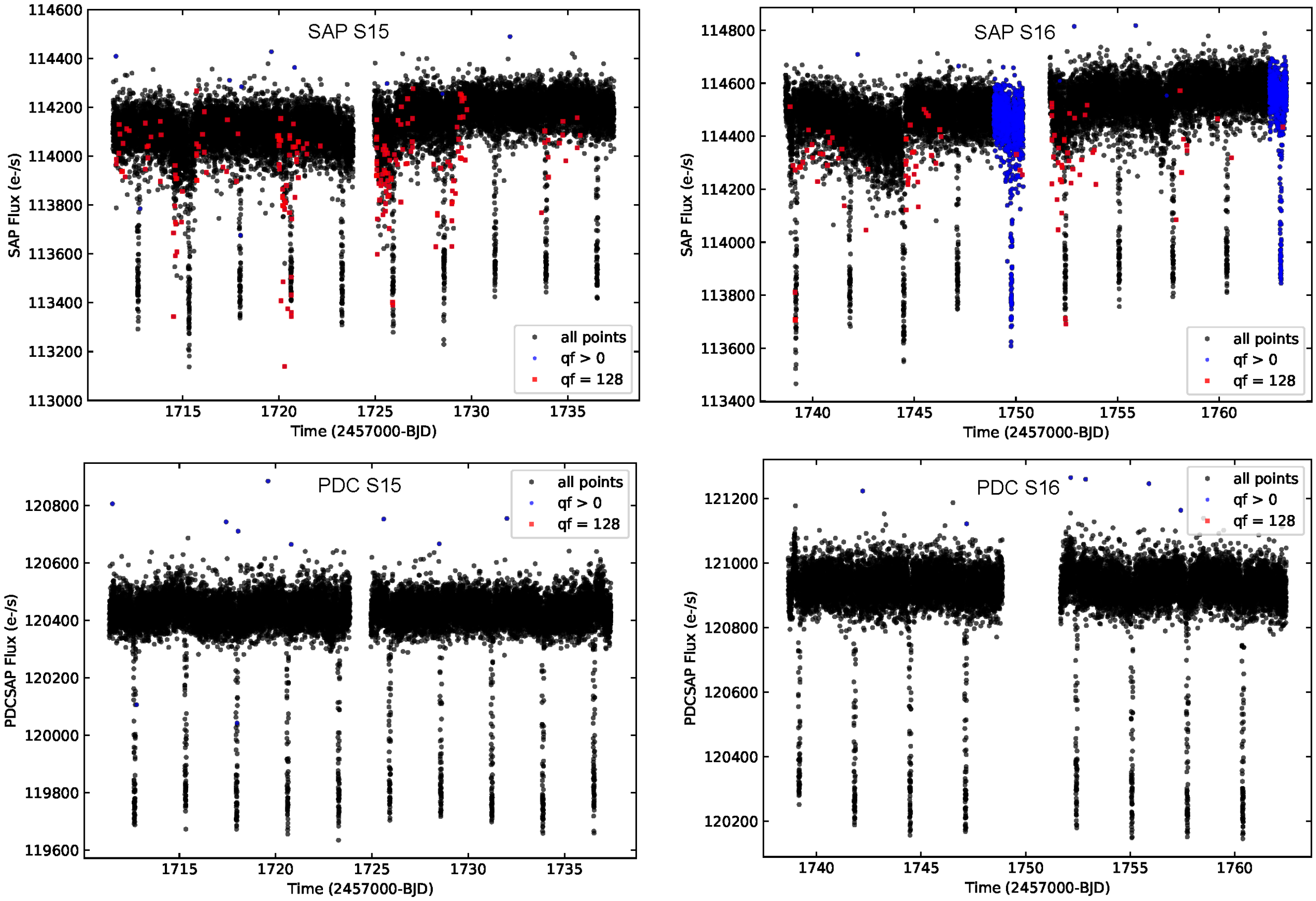

Figure 1. The *TESS* light curves of TOI-1431 from Sectors 15 (left panel) and 16 (right panel). The top panels show the Simple Aperture Photometry (SAP) and the bottom panels show the Presearch Data Conditioning (PDC) versions of the light curves. The circles plotted in blue represent data that have a quality flag greater than 0 (but not equal to 128) and the red squares are data with quality flag equal to 128 (flagged as manual exclude, i.e., the cadence was excluded because of an anomaly). The *TESS* quality flags are described in the *TESS* Data Products Description Document (see, https://archive.stsci.edu/missions/tess/doc/EXP-TESS-ARC-ICD-TM-0014-Rev-F.pdf.

for auto-guiding. We reduced the data and extracted the light curves using the standard MuSCAT2 pipeline (Parviainen et al. 2019), recovering the expected transit signal. Figure 17 in the Appendix shows the transit light curve in all four bands with fits to the transits and systematics, fits to the transits with systematics removed, and the resulting residuals.

2.2.2. *Las Cumbres Observatory Global Telescope*

A full transit of TOI-1431 b was observed on 14 October 2020 from the LCOGT 1.0 m network node at McDonald Observatory near Fort Davis, Texas (LCO-McD) in PANSTARRS Y-band. The SINISTRO camera images were calibrated using the standard LCOGT `BANZAI` pipeline (McCully et al. 2018), and the photometry was extracted using the `AstroImageJ` (`AIJ`) software package (Collins et al. 2017) with 20 pixel (7.8″) apertures. Figure 18 in the Appendix shows a clear transit detection with an individually fitted transit depth of $5.5^{+0.4}_{-0.3}$ ppt, consistent with the SPOC pipeline transit depth of 5.68 ± 0.03 ppt to within 1σ. The model residuals have a standard deviation of 0.58 ppt in 5.4 m bins.

2.3. *Spectroscopic Observations*

We obtained high-resolution spectroscopic observations of TOI-1431 with SONG, SOPHIE, FIES, NRES (TLV and ELP), and EXPRES to establish the planetary nature of the *TESS* transiting candidate and measure its mass. Here we describe the observations from each spectrograph and list the derived radial velocities in Table 5 in the Appendix.

2.3.1. *SONG*

High-resolution spectroscopic observations of TOI-1431 were obtained using the robotic Stellar Observations Network Group (SONG) 1 m Hertzsprung telescope at the Teide Observatory in Tenerife (Andersen

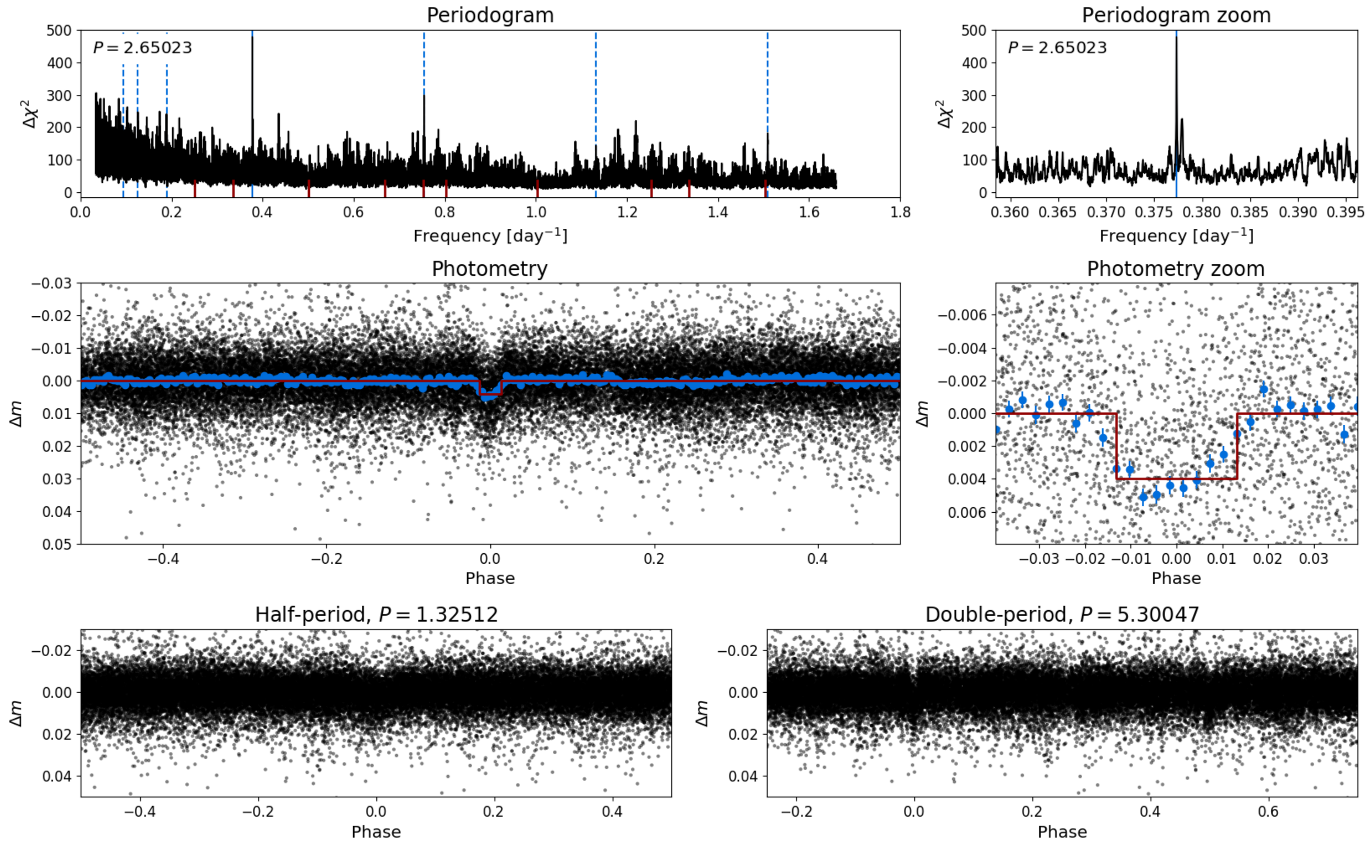

Figure 2. Photometry of TOI-1431 taken from the Multi-site All-Sky CAmeRA (MASCARA) telescope at the Roque de los Muchachos Observatory, La Palma. The top panels are the box least squares periodograms from the MASCARA light curves showing the strongest peak period at 2.65023 d. The middle panels show the phase folded light curve from MASCARA, full-phase on the left and zoomed in on the transit on the right. The blue points represent binned data in 0.003 phase steps, the black points are the original observations in bins of 50 images (320 s), and the red line is the best-fit box least squares model (see, Kovács et al. 2002) used in detecting the transit. The bottom panels show the photometry phase-folded at half and double the period (bottom left and right, respectively) found at the strongest peak in the periodogram. No obvious dip features are seen in the half-period phase-folded plot but two dip features are apparent in double-period phase-folded plot at phase 0 and 0.5, as expected for the transiting planet with a period of 2.65023 d. The MASCARA light curves were not used in the global modeling in `Allesfitter`.

et al. 2014; Fredslund Andersen et al. 2019). In total, 19 spectra were taken with SONG between 06 March 2020 and 29 June 2020. SONG is equipped with a high-resolution coudé échelle spectrograph with wavelength coverage between 4400 − 6900 Å across 51 spectral orders. The observations were taken using the iodine cell to allow for precise wavelength calibration. For each observation, we took a 2400 s exposure in slit mode 6 (slit width 1.2″), providing a spectral resolution of $R = 90,000$, a median count per pixel at 5560 Å of 1795.2 ADU (signal-to-noise ratio of at least 50 per resolution element for all observations), and median radial velocity precision of 29 m s^{-1}.

Before each target observation, calibration frames (including bias frames, flat fields, and ThAr spectra) were taken on the same night and applied to target images. The target observations were then reduced and the spectra extracted with a pipeline written in Python. This pipeline uses a C++ implementation of the optimal extraction method from Ritter et al. (2014). We also acquired observations of the bright fast-rotating star HR 5191 that was used as an intrinsic stellar template for determining the spectral-line-spread function of the spectrograph and to deconvolve a high signal-to-noise spectrum of TOI-1431 taken without the iodine cell. We then analyzed the extracted spectra using the iSONG pipeline (Antoci et al. 2013) to produce radial velocities (given in Table 5 and shown in Figure 3), following the procedure of Grundahl et al. (2017).

2.3.2. *SOPHIE*

TOI-1431 was observed with the fiber-fed SOPHIE high-resolution échelle spectrograph on the 1.93 m telescope at the Haute-Provence Observatory (Perruchot et al. 2008, 2011) between 18 December 2019 and 12 January 2020. We collected a total of eight spectra in the high-resolution (HR) mode ($R = 75,000$ at 5500 Å). The second SOPHIE aperture allowed us to check that there was no background sky pollution. Thorium-argon calibration spectra were taken at the start of each night of the observations to determine the wavelength calibration zero point, as well as Fabry-Pérot étalon spectra regularly during the nights to monitor any possible instrumental drift. The spectra cover the wavelength range from 3872 – 6943 Å across 41 spectral orders, of which 39 were extracted and used for computing the radial velocities. The exposure times ranged from 214 and 490 s, resulting in a uniform signal-to-noise ratio for each observation of 50 per resolution element at 5500 Å and median Doppler velocity precision of 7 $\mathrm{m\,s^{-1}}$.

The spectroscopic data were reduced and then extracted using the standard SOPHIE pipeline (Bouchy et al. 2009), which performs optimal order extraction, cosmic-ray rejection, and wavelength calibration. Radial velocities were computed using the cross-correlation technique and a numerical binary mask corresponding to a F0 spectral type star (e.g., see, Courcol et al. 2015), the closest available binary mask to TOI-1431's spectral type. Table 5 list the radial velocities from SOPHIE and they are shown in Figure 3. The width of the cross-correlation function allows us to measure the rotational velocity of the star as $v \sin i = 6.0 \pm 0.2$ $\mathrm{km\,s^{-1}}$.

2.3.3. *FIES*

We acquired 52 spectra of TOI-1431 using the FIbre-fed Échelle Spectrograph (FIES; Frandsen & Lindberg 1999; Telting et al. 2014) at the 2.56 m Nordic Optical Telescope (NOT; Djupvik & Andersen 2010) of Roque de los Muchachos Observatory (La Palma, Spain). The observations were carried out between 27 November 2019 and 20 June 2020 (UT). We used the FIES high-resolution mode, which provides a resolving power of $R = 67\,000$ in the spectral range 3760–8220 Å. We traced the RV drift of the instrument by acquiring long-exposure ThAr spectra ($T_{\rm exp} \approx 90$ s) immediately before and after each science exposure. The exposure time was set to 300–900 s, depending on the sky conditions and scheduling constraints. The data reduction follows the steps of Buchhave et al. (2010) and includes optimal extraction of the spectrum and interpolation of the ThAr wavelength solutions. The SNR per pixel at 5500 Å of the extracted spectra is in the range 42–127. We cross-correlate each observation order-by-order in velocity space against the strongest exposure of the star (BJD=2 458 995.703 476). Finally, the radial velocity of each observation is measured from the peak of the summed cross-correlation function and transformed to the barycentric frame. The uncertainties for the derived radial velocities range 7.2–19.1 $\mathrm{m\,s^{-1}}$ with a mean value of 12.2 $\mathrm{m\,s^{-1}}$.

2.3.4. *NRES*

We triggered observations of TOI-1431 on the Network of Robotic Echelle Spectrographs (NRES) (Siverd et al. 2018b), operated by the LCOGT (Brown et al. 2013b). NRES consists of four similar spectrographs with two in the Northern Hemisphere and two in the Southern. The spectrographs cover the wavelength range from 380 to 860 nm with a resolution of R$\sim$53,000. They are fibre-fed, where one fibre observes the science target and the second fibre is used for the wavelength calibration source. In the case of NRES the calibration source is a ThAr lamp.

Due to the target's Northern declination, TOI-1431 was accessible and observed by the units at the Wise Observatory (TLV) and the McDonald Observatory (ELP). We obtained a total of 34 spectra. For spectral classification we used the standard NRES pipeline in combination with SpecMatch-Synth code[2]. In order to obtain high precision RV measurements, we processed the spectra using an adapted version of the CERES pipeline (Brahm et al. 2017).

2.3.5. *EXPRES*

We observed TOI-1431 with the Extreme PREcision Spectrometer (EXPRES) (Jurgenson et al. 2016) which was recently commissioned at the 4.3 m Lowell Discovery Telescope (DCT) (Levine et al. 2012). EXPRES is a vacuum-stabilized and fiber-fed optical spectrograph, operating between 380 and 780 nm at a resolution of $R \sim 137,500$. It achieves a single-measurement radial velocity precision of approximately 30 $\mathrm{cm\,s^{-1}}$ at SNR of 250 per pixel (Petersburg et al. 2020). The wavelength solution is determined from both a ThAr lamp and a Menlo Systems laser frequency comb (LFC). Recent performance benchmarks and science results are shown by Blackman et al. (2020) and Brewer et al. (2020), and the radial velocity pipeline is discussed by Petersburg et al. (2020). For TOI-1431, we acquired 15 observations with EXPRES and achieved a mean radial velocity precision of 2.1 $\mathrm{m\,s^{-1}}$.

2.4. *High-Contrast Imaging Observations*

We obtained high angular resolution imaging of TOI-1431 using the NIRC2 instrument on the Keck II. The observations were taken on the night of 09 September

[2] https://github.com/petigura/specmatch-syn

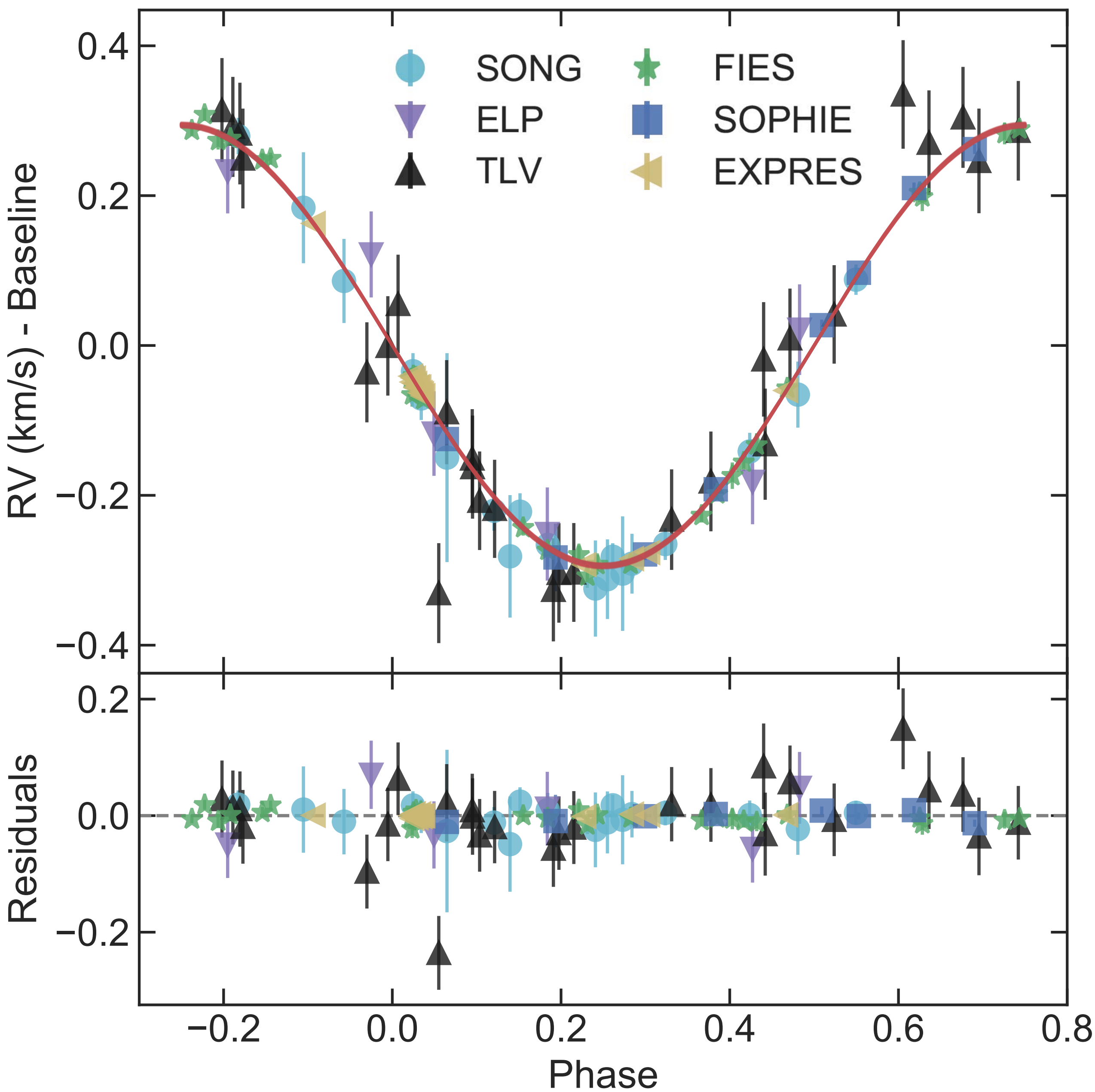

Figure 3. Radial velocity measurements of TOI-1431 b/MASCARA-5 b as a function of orbital phase. The radial velocities from SONG, NRES (ELP and TLV), FIES, SOPHIE, and EXPRES are represented by the cyan colored circles, purple triangles pointed down, black triangles pointed up, green stars, blue squares, and gold triangles pointed to the left, respectively. A random selection of 20 radial velocity curves drawn from the posterior of the Nested Sample modeling are plotted as the red lines. The bottom panel shows the residuals between the data and the best-fit (posterior median) model.

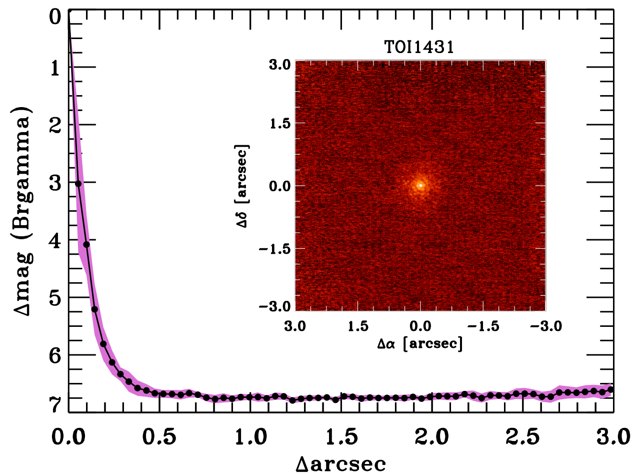

Figure 4. The 5σ **detection sensitivity and AO image** from Keck II NIRC2 high angular resolution imaging of TOI-1431 in the Brgamma-band. The orientation of the AO image has North pointed up and East to the left. No stars were detected within $3''$ of TOI-1431.

2020 UTC under clear skies, very good seeing conditions of $\sim 0.4''$, and at an airmass of 1.25. The resulting 5σ detection sensitivity and adaptive optics (AO) image from the NIRC2 observations are plotted in Figure 4. No nearby companions or background sources were detected within $3''$ of TOI-1431.

3. HOST STAR PROPERTIES

TOI-1431/MASCARA-5 (HD 201033) is a bright (V = 8.049) Am (chemically peculiar) type star (Figueras et al. 1991; Renson et al. 1991) with a *Gaia* DR2 parallax of 6.686 ± 0.046 mas (Gaia Collaboration et al. 2018a) and distance of $149.6^{+1.1}_{-1.0}$ pc. The star has a radius of $1.92 \pm 0.03\,R_\odot$, mass of $1.89^{+0.09}_{-0.08}\,M_\odot$, surface gravity of $\log g = 4.15^{+0.03}_{-0.03}$ dex, effective temperature of 7680^{+350}_{-230} K, metallicity of $[Fe/H] = 0.43^{+0.19}_{-0.26}$ dex, and luminosity of $11.6^{+2.0}_{-1.1}\,L_\odot$, derived from an analysis of the broadband spectral energy distribution (SED) and the Yonsei Yale (YY) stellar evolutionary models (Yi et al. 2001) using `EXOFASTv2` (Eastman et al. 2019) as discussed in Section 3.1. We also derive independent values for the effective temperature and metallicity from the analysis of SONG, SOPHIE, and FIES spectra in Section 3.2.

Table 1. Stellar parameters for HD 201033 as used in this work. **Notes.**–†Priors used in the Allesfitter analysis. ‡Preferred solution for the stellar and spectroscopic parameters. *Upper limit on the V-band extinction from Schlegel Dust maps.

Parameter	Value	Source
R.A. (hh:mm:ss)	21:04:48.89	(1) *Gaia* DR2
Decl. (dd:mm:ss)	55:35:16.88	(1) *Gaia* DR2
μ_α (mas yr^{-1})	11.74 ± 0.08	(1) *Gaia* DR2
μ_δ (mas yr^{-1})	23.87 ± 0.06	(1) *Gaia* DR2
Parallax (mas)	6.686 ± 0.046	(1) *Gaia* DR2
Luminosity ($L_\odot$)	$10.69 \pm 0.10^\ddagger$	(1) *Gaia* DR2
A_V (mag)	$1.099\ (\leq 3.491)^\star$	(2) Schlegel Dust maps
Distance (pc)	$149.6^{+1.1}_{-1.0}$	(1) *Gaia* DR2
Spectral type	Am C	(3,4) A-type star catalogs
Broadband Magnitudes:		
B_T (mag)	8.368 ± 0.016	(5) Tycho
V_T (mag)	8.049 ± 0.011	(5) Tycho
TESS (mag)	7.798 ± 0.006	(6) *TESS* TIC v8
J (mag)	7.541 ± 0.030	(7) 2MASS
H (mag)	7.452 ± 0.040	(7) 2MASS
K_s (mag)	7.439 ± 0.030	(7) 2MASS
*WISE*1 (mag)	7.335 ± 0.034	(8) WISE
*WISE*2 (mag)	7.430 ± 0.019	(8) WISE
*WISE*3 (mag)	7.446 ± 0.015	(8) WISE
*WISE*4 (mag)	7.371 ± 0.096	(8) WISE
Gaia (mag)	7.976 ± 0.001	(1) *Gaia* DR2
$Gaia_{BP}$ (mag)	8.123 ± 0.001	(1) *Gaia* DR2
$Gaia_{RP}$ (mag)	7.772 ± 0.001	(1) *Gaia* DR2
Stellar Properties from SED & YY Tracks:		
$T_{\rm eff}$ (K)	$7690^{+400\ \dagger,\ddagger}_{-250}$	(9) `EXOFASTv2`; this paper
$\log g$ (dex)	$4.15 \pm 0.04^\ddagger$	(9) `EXOFASTv2`; this paper
[Fe/H] (dex)	$0.43^{+0.20}_{-0.28}$	(9) `EXOFASTv2`; this paper
$R_\star$ ($R_\odot$)	$1.92 \pm 0.07^{\dagger,\ddagger}$	(9) `EXOFASTv2`; this paper
$M_\star$ ($M_\odot$)	$1.90^{+0.10\ \dagger,\ddagger}_{-0.08}$	(9) `EXOFASTv2`; this paper
$\rho_\star$ (g cm^{-3})	0.38 ± 0.05	(9) `EXOFASTv2`; this paper
$L_\star$ ($L_\odot$)	$11.7^{+2.3}_{-1.2}$	(9) `EXOFASTv2`; this paper
Age (Gyr)	$0.29^{+0.32\ \ddagger}_{-0.19}$	(9) `EXOFASTv2`; this paper
Spectroscopic Properties from SONG spectra:		
$T_{\rm eff}$ (K)	6764 ± 120	(10,11) iSpec; this paper
$\log g$ (dex)	2.76 ± 0.26	(10,11) iSpec; this paper
[M/H] (dex)	-0.15 ± 0.10	(10,11) iSpec; this paper
[α/H] (dex)	-0.27 ± 0.10	(10,11) iSpec; this paper
$v \sin i$ (km s^{-1})	7.1 ± 1.0	(10,11) iSpec; this paper
Spectroscopic Properties from SOPHIE spectra:		
$T_{\rm eff}$ (K)	6950 ± 60	(12) FASMA; this paper
$\log g$ (dex)	4.72 ± 0.08	(12) FASMA; this paper
[Fe/H] (dex)	$0.09 \pm 0.03^\ddagger$	(12) FASMA; this paper
$v \sin i$ (km s^{-1})	$6.0 \pm 0.2^\ddagger$	CCF; this paper
Spectroscopic Properties from FIES spectra:		
$T_{\rm eff}$ (K)	6910 ± 50	(13) SPC; this paper

Table 1 *continued*

Table 1 *(continued)*

Parameter	Value	Source
$\log g$ (dex)	3.29 ± 0.10	(13) SPC; this paper
[M/H] (dex)	0.03 ± 0.08	(13) SPC; this paper
$v \sin i$ (km s^{-1})	9.2 ± 0.5	(13) SPC; this paper

References—1. Gaia Collaboration et al. (2018b); 2. Schlafly & Finkbeiner (2011); 3. Figueras et al. (1991); 4. Renson et al. (1991); 5. Høg et al. (2000); 6. Stassun et al. (2019); 7. Cutri et al. (2003); 8. Cutri et al. (2013); 9. Eastman et al. (2019) ; 10. Blanco-Cuaresma et al. (2014); 11. Blanco-Cuaresma (2019); 12. Tsantaki et al. (2018); 13. Buchhave et al. (2012)

3.1. *SED Analysis*

We performed a SED analysis of TOI-1431 using `EXOFASTv2` to derive stellar parameters independent of those from spectroscopy. We used broadband photometry obtained from the Tycho (Høg et al. 2000), 2MASS (Cutri et al. 2003), WISE (Cutri et al. 2013), and *Gaia* (Gaia Collaboration et al. 2018b) catalogs for the fitting of the SED (Figure 5). Gaussian priors were placed on the parallax from *Gaia* DR2, adding 82 μas to correct for the systematic offset found by Stassun & Torres (2018) and adding the 33 μas uncertainty in their offset in quadrature to the *Gaia*-reported uncertainty. We applied an upper limit on the V-band extinction from the Schlafly & Finkbeiner (2011) dust maps at the location of TOI-1431 as well as an upper limit on the dilution effects of nearby stars as reported in the *TESS* SPOC light curve file. The YY stellar evolutionary models were used instead of the default MESA Isochrones and Stellar Tracks (MIST) to determine the stellar radius ($R_\star$), mass ($M_\star$), effective temperature ($T_{\rm eff}$), luminosity ($L_\star$), metallicity ([Fe/H]), surface gravity ($\log g$), and age of TOI-1431, which are given in Table 1. We found that using the MIST models resulted in many of the Markov Chain Monte Carlo (MCMC) steps reaching the [Fe/H] grid's upper limit of 0.5 dex while the MCMC chains never reached the [Fe/H] upper limit of 0.78 dex using the YY tracks. The YY evolutionary models are better suited for hot metal rich stars such as TOI-1431.

From the best-fit Kurucz stellar atmosphere model from the SED and the best-fitting YY stellar evolutionary model (Figure 6), we find that TOI-1431 is a very hot and metal rich A-type star with $R_\star = 1.92 \pm 0.07\,{\rm R}_\odot$, $M_\star = 1.90^{+0.10}_{-0.08}\,{\rm M}_\odot$, $T_{\rm eff} = 7690^{+400}_{-250}\,{\rm K}$, $\log g = 4.15 \pm 0.04$ (where g is in units of cm s^{-2}), and $[{\rm Fe/H}] = 0.43^{+0.20}_{-0.28}$ dex. The effective temperature found for this star makes it one of the hottest known exoplanet hosts. These stellar parameters (in particular $T_{\rm eff}$, $\log g$, and metallicity), however, are in strong disagreement with the spectroscopic parameters derived from the analysis of the SONG, SOPHIE, and FIES data. The source of this disagreement is likely due to

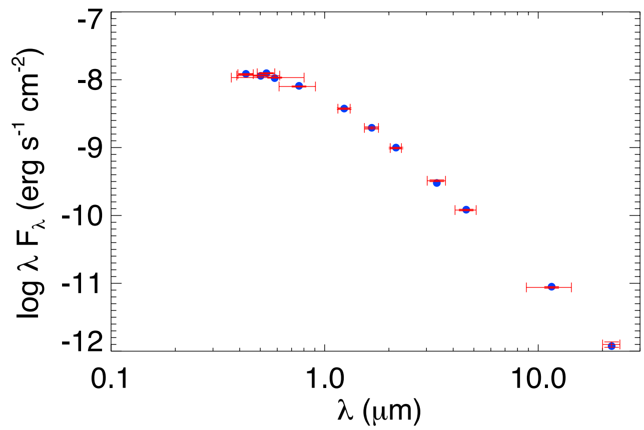

Figure 5. The SED for TOI-1431. The red symbols are the broadband photometric measurements used in the SED analysis (provided in Table 1) with the horizontal uncertainty bars representing the effective width of the passband. The blue symbols are the model fluxes from the best-fit Kurucz atmosphere model.

the "anomalous luminosity effect" observed in Am stars (e.g., Bolton 1971) such as TOI-1431, which we discuss further in Section 6.1. The $\log g$ derived from the SED fit is in good agreement with the value obtained from the stellar density ($\log g \sim 4.17$ dex) from fitting the transits, and we have therefore adopted this value along with the values for $T_{\rm eff}$, $R_\star$, and $M_\star$ as the preferred values for the star.

3.2. *Spectroscopy*

We used the iSpec spectral analysis tool (Blanco-Cuaresma et al. 2014; Blanco-Cuaresma 2019) to derive the effective temperature, surface gravity, rotational velocity, alpha elemental abundance ([α/H]), and overall metallicity ([M/H]) of TOI-1431 from the reduced and stacked SONG spectra. The iSpec synthetic grid was configured to incorporate a MARCS atmospheric model (Gustafsson et al. 2008) and the SPECTRUM (Gray & Corbally 1994) radiative transfer code. [M/H] and [α/H] were derived using version 5.0 of *Gaia*-ESO Survey's (GES) line-list (Heiter et al. 2015) normalized by solar values obtained by Asplund et al. (2009). Initial values for $T_{\rm eff}$, $\log g$, and [M/H] as determined by the SED analysis with `EXOFASTv2` (see Section 3.1) were used to construct the synthetic spectra fit. From the iSpec analysis of the SONG spectra, we find that TOI-1431 has a $T_{\rm eff} = 6764 \pm 120$ K, $\log g = 2.76 \pm 0.26$ dex, $[{\rm M/H}] = -0.15 \pm 0.10$ dex, $[\alpha/{\rm H}] = -0.27 \pm 0.10$ dex, and $v \sin i = 7.1 \pm 1.0$ km s^{-1}. These results would seem to suggest that the star is quite evolved, is slightly metal poor, and is deficient in α elements. However, $T_{\rm eff}$ and $\log g$, in particular, are in very strong disagreement with

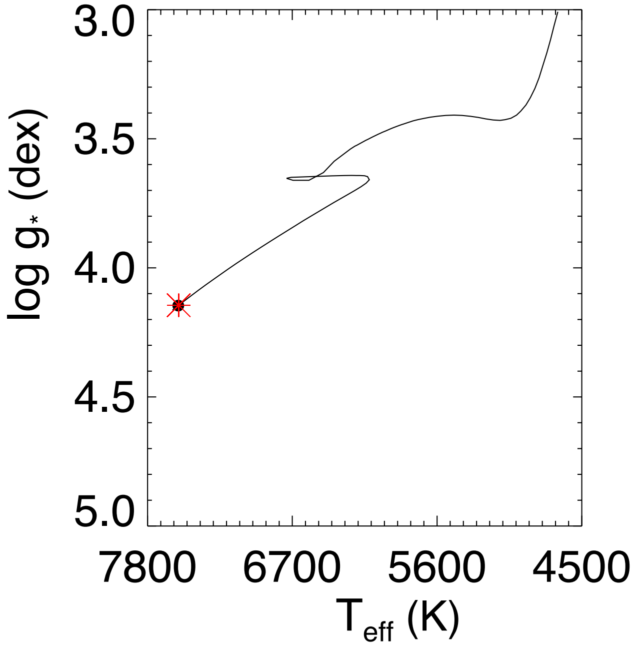

Figure 6. The YY mass track for TOI-1431. The black line represents the mass track interpolated at the model values for $M_\star$, [Fe/H], and age. The black circle is the best-fit model value for $T_{\rm eff}$ and $\log g$ while the red asterisk is the best-fit model age along the track. The black circle and red asterisk almost perfectly overlap indicating excellent consistency among all the components of the global model.

the results obtained from the SED analysis as a consequence of the nature of the host being an Am star (see discussion in Section 6.1).

The atmospheric stellar parameters $T_{\rm eff}$, $\log g$, and [Fe/H] were derived from the SOPHIE spectra for TOI-1431 using the *FASMA* spectral synthesis package (Tsantaki et al. 2018). We provided initial stellar parameters for $T_{\rm eff}$, $\log g$, and [Fe/H] from the SED analysis with `EXOFASTv2` as a starting point of the spectral synthesis in *FASMA*. The synthetic spectra were created using the radiative transfer code, MOOG (Sneden 1973), and the model atmospheres grid was generated by the ATLAS-APOGEE (Kurucz 1993), MARCS (Gustafsson et al. 2008), and ATLAS9 (Mészáros et al. 2012) models. The line list used to determine the stellar parameters comes from the Vienna Atomic Line Database (VALD, Piskunov et al. 1995; Ryabchikova et al. 2015) and includes all of the iron lines in the regions $5399-5619$ Å and $6347-6790$ Å as well as all the atomic and molecular lines within intervals of ± 2 Å of the iron lines. From this analysis with the SOPHIE spectra, we find the star has $T_{\rm eff} = 6950 \pm 60$ K, $\log g = 4.72 \pm 0.08$ dex, and $[{\rm Fe/H}] = 0.09 \pm 0.03$ dex, consistent with a late A-type main-sequence star that is modestly metal rich. We have adopted the [Fe/H] value derived here as the preferred value for the star's iron abundance.

The stellar parameters for this star were also derived from the FIES spectra using the stellar parameter classification (SPC) technique (Buchhave et al. 2012; Torres et al. 2012; Buchhave et al. 2014). To derive $T_{\rm eff}$, $\log g$, $v \sin i$, and [M/H] for this star using SPC, we cross-correlated the reduced and the stacked FIES spectra against a library of synthetic spectra calculated from the Kurucz model atmospheres (Castelli & Kurucz 2003). The synthetic spectra covers the wavelength range from $5050-5360$ Å, of which five of the FIES echelle orders span that region and could be used for the spectral analysis. The best-fit values were determined by finding the maximum of the cross-correlation coefficient as a function of the stellar parameters. The results of the SPC analysis on the FIES spectra gives $T_{\rm eff} = 6910 \pm 50$ K, $\log g = 3.29 \pm 0.10$ dex, $[{\rm M/H}] = 0.03 \pm 0.08$ dex, and $v \sin i = 9.2 \pm 0.5$ km s^{-1}, which suggest an A-type subgiant star with solar metallicity. It should be noted that SPC was not designed for hot stars such as TOI-1431 and that surface gravities are often poorly constrained by spectral analyses (e.g., see, Sozzetti et al. 2007; Winn et al. 2008).

The spectral analyses carried out on the SONG, SOPHIE, and FIES spectra give significantly different results for the host star properties, and in particular for the surface gravity. However, the stellar density (and surface gravity) determined from the SED and transit light curve analysis are in good agreement with each other. Winn et al. (2008) has demonstrated that stellar densities can be more accurately determined through transit light curve analysis and should be preferred over those derived through spectroscopy if there are strong disagreements between them. In this light, we therefore have adopted the $T_{\rm eff}$, $\log g$, $R_\star$, and $M_\star$ from the SED analysis as the preferred values for the star.

4. MODELLING AND RESULTS

4.1. *TESS Light Curve Analysis*

To determine the system parameters for TOI-1431 and its planet, including the planet's thermal emissions and day-night temperature contrast, we used `Allesfitter` (Günther & Daylan 2019, 2020) to perform an analysis of the *TESS* SAP, multi-scale MAP corrected PDC, and single-scale MAP corrected PDC photometry. For this analysis, Gaussian priors were placed on the stellar parameters $R_\star$, $M_\star$, and $T_{\rm eff}$ from the SED and YY isochrones fitting using `EXOFASTv2`. We also applied a Gaussian prior on the dilution parameter (D_0) from the *TESS* SPOC light curve parameter CROWDSAP, after transforming the CROWDSAP value to conform to the definition of the dilution parameter used in `Allesfitter`. For the other physical model parameters, we used uniform priors with reasonable boundaries and starting values. These parameters include the planet-to-star radius ratio ($R_p/R_\star$), the ratio of the sum of the planet and star radii to the semi-major axis ($(R_\star + R_p)/a_p$), cosine of the inclination angle ($\cos i_p$), mid-transit time ($T_{0;b}$), orbital period (P_p), eccentricity ($\sqrt{e_p}\cos\omega_p$ and $\sqrt{e_p}\sin\omega_p$), quadratic limb darkening coefficients (q_1 and q_2), and surface brightness ratio (J_p).

Close inspection of the *TESS* light curves reveals periodic photometric modulations that are synchronized with the orbital period of the planet. These phase curve variations are driven by the changing viewing angle of the planet and the planet–star gravitational interaction. There are three main components to the phase curve that can be detected in visible-light photometry (see detailed review in Shporer 2017): (1) the atmospheric brightness modulation, which arises due to the variations in atmospheric temperature, thermal emission, and reflected starlight across the surface of a tidally-locked planet, (2) ellipsoidal distortion of the host star due to the tidal bulge raised by the orbiting planet, and (3) beaming, i.e., modulations in the star's flux within the band-pass due primarily to the radial velocity driven Doppler shifting of the stellar spectrum. Setting the zeropoint of orbital phase at mid-transit, these three phase curve modulations appear as, to the leading order, the cosine of the fundamental frequency, the cosine of the first harmonic, and the sine of the fundamental.

In this work, we used `Allesfitter` to fit for these phase curve terms by including free parameters for the respective full amplitudes: $A_{\text{atmospheric}}$, $A_{\text{ellipsoidal}}$, and A_{beaming}. Similar methodologies have been used in extensive previous phase curve analyses of *TESS*-observed exoplanet systems (e.g., Shporer et al. 2019; Wong et al. 2020a,b,c; Daylan et al. 2021).

4.1.1. *Multi-scale MAP PDC Photometry*

We started the analysis using the *TESS* multi-scale MAP corrected PDC light curve (after removing all quality-flagged data and outliers as described in Section 2.1) since most of the instrumental systematics are removed by the SPOC PDC pipeline from the use of co-trending basis vectors and flux corrections due to crowding from other stars (e.g., see Stumpe et al. 2014). This results in a cleaner light curve compared to the SAP version while still preserving astrophysical signals on timescales shorter than the orbital period of TOI-1431 b, important for phase curve and secondary eclipse analysis. The PDC light curve was analyzed using two approaches. The first approach was detrending each light curve segment with a long-window function rspline (knot spacing 4 times longer than the orbital period of the planet to preserve phase curve) using the `Wōtan` (Hippke et al. 2019) Python package before fitting the light curve in `Allesfitter` using the zeroth order sample baseline flux offset parameter. The second approach was to use the hybrid cubic spline detrending option in `Allesfitter` during the light curve fitting process.

For both approaches, we fit the full phase curve (using the three sinusoidal terms, as described above) and secondary eclipse on the light curve segments using a MCMC that ran until convergence (all chains are > 42 times their autocorrelation lengths). In the case of TOI-1431, atmospheric modulation is expected to be the largest contributor to the phase curve. These phase curve parameters were coupled across all the light curve segments so as to only sample one set of values and uncertainties for each of them. This was done since the light curve segments come from the same instrument that `Allesfitter` treats as separate instruments in the analysis. For the same reason, we also coupled the parameters D_0, q_1 and q_2, J_p, and flux error scaling ($\ln \sigma_{TESS}$).

Figure 7 is the resulting phase-folded and detrended PDC light curve of TOI-1431, overplotted with 20 light curve models drawn from the MCMC posteriors when using cubic spline detrending simultaneously during the fitting process. Both light curve analysis approaches (detrending before and during the fitting) give similar results. It is apparent in the residuals to the best-fit transit model that there are two significant dip features in the light curve (~ 200 ppm depth), one starting ~ 1 hr before transit ingress and continuing until just after the start of ingress and another starting just prior to the end of egress with a duration of ~ 1 hr. These dip features are present in both detrending approaches as well as the Data Validation (DV) light curve provided in the Data Validation Report Summary available on exo.MAST.

Further investigations revealed the source of the dip features to be a wavelet artifact caused by the multi-scale MAP correction applied by PDC. Multi-scale MAP PDC (Stumpe et al. 2014) divides each light curve into three wavelet band passes and then performs a MAP-like (Maximum A Posteriori) correction in each using separate cotrending basis vectors derived within each band-pass. A fit to neighboring targets is used as the Bayesian prior during the a-posteriori fit. Normally, multi-scale MAP performs better than single-scale MAP (where no band-splitting is performed, Smith et al. 2012) for removing long period systematics while preserving signals at transit scales. However, there is a mechanism where

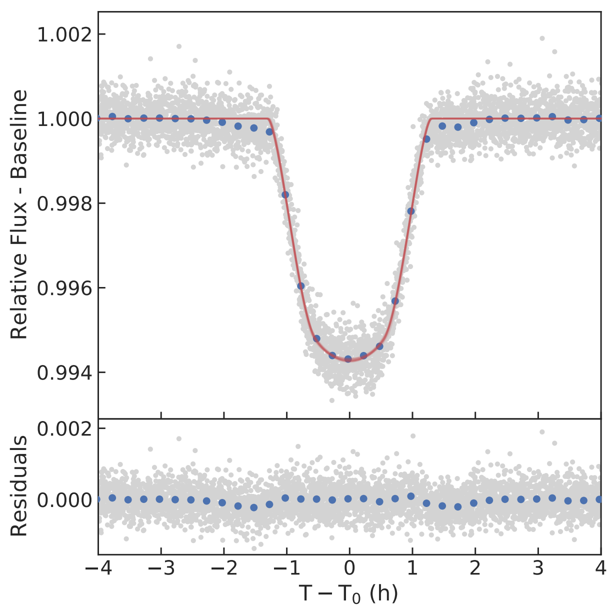

Figure 7. Phase-folded and detrended *TESS* PDC light curve of TOI-1431 (Sectors 15 and 16) from the simultaneous hybrid cubic spline detrending model, focusing on the transit. Systematics and other quality-flagged data (as shown in Figure 1) that are the result of, for example, spacecraft pointing anomalies have been removed prior to performing the analysis on the light curve. The blue points are binned at a cadence of 15 m and the red solid lines are 20 light curve models drawn from the posteriors of the Markov Chain Monte Carlo (MCMC) analysis in `Allesfitter`. Dip features starting $\sim$ 1 hr before and after transit ingress and egress, respectively, are apparent in the light curve and were introduced during the PDC multi-scale MAP cotrending process. These dip features are not present in the single-scale MAP corrected PDC and SAP versions of the light curve (see Figure 8). Since the PDC light curve is contaminated with the dip systematics that can potentially bias the results, we chose to use the SAP light curve for our analysis.

multi-scale MAP can slightly corrupt a very deep transit in a light curve with little long period systematics, such as we see in TOI-1431. The single-scale MAP corrected light curve was found to not contain the dip features and we chose to perform the analysis on that light curve.

4.1.2. *Single-scale MAP PDC Photometry*

The `Allesfitter` analysis of the pre-cleaned (as described in Section 2.1) single-scale MAP corrected PDC light curve segments follows the same procedure as with the multi-scale MAP corrected PDC light curves, but with a few modifications to ensure accurate and precise results using the less optimal single-scale MAP corrected PDC photometry. We experimented with several different detrending techniques in our analysis, including: (1) baseline flux offset, (2) rspline detrending prior to the light curve fitting with a baseline flux offset, (3) hybrid cubic spline detrending run simultaneously with the light curve fitting, and (4) a red noise detrending model using a Matérn 3/2 Gaussian Processes (GP) kernel run simultaneously with the light curve fitting. For the GP parameters, we applied uniform priors with reasonable boundaries and starting values on the flux offset, characteristic amplitude, and characteristic length scale. These parameters were also coupled across the light curve segments so that a single GP model is sampled at every sampling step. The lower boundary on the characteristic length scale term was set to three times the planet's orbital period to ensure that the GP preserves the phase curve while still removing most of the remaining systematics present in the PDC light curve segments. For all the other stellar, planetary, and orbital parameters, we applied the same priors and boundaries for this analysis as we used in the previous analysis of the multi-scale MAP corrected PDC photometry.

We ran MCMC fits until convergence for the four different detrending techniques. We then used the best-fit parameter values found from the MCMC as starting values in subsequent Nested Sampling fits to estimate the Bayesian evidence for use in a robust comparison of the four detrending models. We used the default `Allesfitter` settings for the nested sampling fits (see Günther & Daylan 2020) that ran until they reached the convergence criterion threshold of $\Delta \ln Z \leq 0.01$.

The results from the Nested Sampling fits are in good agreement with the MCMC results to within 1σ. Comparing the Bayesian evidence of the Nested Sampling models, we find that the hybrid cubic spline detrending run simultaneously with the light curve fitting is decisively favored over the second most favored model, the red noise GP detrending model, with a Bayes model comparison factor of $\ln R = 119$. Figure 8 shows the resulting phase folded and detrended single-scale MAP PDC light curve of TOI-1431, focused on the transit, from the simultaneous cubic spline detrending Nested Sampling model. Unlike the multi-scale MAP PDC light curve shown in Figure 7, there is no evidence of the strange dip features near the transit, motivating our decision to use the results derived from the single-scale MAP version of light curve analysis.

Table 2 gives both the fitted and derived parameters. We find that TOI-1431 hosts an inflated highly irradiated Jovian planet with a radius of $R_p = 1.51 \pm 0.06\,\mathrm{R_J}$ ($16.9^{+0.7}_{-0.6}\,\mathrm{R_\oplus}$), high equilibrium temperature of $T_{\rm eq} = 2370 \pm 100\,\mathrm{K}$ (assuming zero Bond albedo), and a circular orbit with a period of $P = 2.65022 \pm 0.00001\,\mathrm{d}$. There is also a clear signature of the secondary eclipse (occultation, i.e., when the planet passes behind the

Table 2. Median values and 68% confidence interval of the fitted and derived parameters for TOI-1431b from the nested sampling `Allesfitter` analysis of the *TESS* single-scale MAP PDC light curve from the simultaneous cubic spline detrending model. We also include the median values and 68% confidence interval of the same fitted and derived parameters from the analysis of the *TESS* SAP photometry using the simultaneous cubic spline detrending model. †Preferred solution for the fitted and derived parameters.

Parameter	Description	Value (with PDC)†	Value (with SAP)
Fitted parameters			
$R_p/R_\star$	Radius ratio	$0.0805^{+0.0015}_{-0.0008}$	$0.0822^{+0.0021}_{-0.0012}$
$(R_\star + R_p)/a$	Radii sum to semi-major axis	$0.206^{+0.003}_{-0.006}$	0.205 ± 0.004
$\cos i_p$	Cosine of inclination	$0.166^{+0.005}_{-0.010}$	$0.164^{+0.006}_{-0.005}$
T_0	Mid transit time ($\mathrm{BJD_{TDB}}$)	$2458739.17736 \pm 0.00007$	$2458739.17734 \pm 0.00010$
P_p	Orbital period (d)	2.65022 ± 0.00001	2.65024 ± 0.00002
$\sqrt{e}\cos\omega$	Eccentricity term	-0.01 ± 0.02	0.01 ± 0.03
$\sqrt{e}\sin\omega$	Eccentricity term	$-0.09^{+0.12}_{-0.13}$	$0.02^{+0.10}_{-0.09}$
D_0	Dilution	$0.0046^{+0.0004}_{-0.0005}$	$0.0048^{+0.0006}_{-0.0005}$
q_1	Transformed limb darkening	0.23 ± 0.05	$0.46^{+0.13}_{-0.09}$
q_2	Transformed limb darkening	$0.35^{+0.31}_{-0.22}$	$0.28^{+0.34}_{-0.19}$
J_p	Surface brightness ratio	$0.007^{+0.003}_{-0.002}$	$0.007^{+0.004}_{-0.003}$
A_{beaming}	Phase curve term (ppt)	$0.0011^{+0.0016}_{-0.0007}$	0.010 ± 0.005
$A_{\mathrm{atmospheric}}$	Phase curve term (ppt)	0.077 ± 0.008	0.10 ± 0.01
$A_{\mathrm{ellipsoidal}}$	Phase curve term (ppt)	0.028 ± 0.006	$0.040^{+0.009}_{-0.010}$
$\ln \sigma_{\mathrm{TESS}}$	Flux error scaling (ln rel.flux.)	-7.779 ± 0.004	-7.546 ± 0.004
Derived parameters			
$R_\star/a$	Host radius to semi-major axis	$0.191^{+0.003}_{-0.005}$	$0.190^{+0.004}_{-0.003}$
$a/R_\star$	Semi-major axis to host radius	$5.25^{+0.15}_{-0.09}$	$5.26^{+0.10}_{-0.11}$
R_{p}	Planet radius ($\mathrm{R_\oplus}$)	$16.9^{+0.7}_{-0.6}$	17.3 ± 0.7
R_{b}	Planet radius ($\mathrm{R_J}$)	1.51 ± 0.06	1.55 ± 0.06
a	Semi-major axis (AU)	0.047 ± 0.002	0.047 ± 0.002
i	Inclination (deg)	$80.4^{+0.6}_{-0.3}$	$80.6^{+0.3}_{-0.4}$
e	Eccentricity	$0.010^{+0.036}_{-0.009}$	$0.005^{+0.016}_{-0.004}$
ω	Argument of periastron (deg)	260^{+10}_{-160}	110^{+180}_{-40}
b_{tra}	Impact parameter	$0.881^{+0.003}_{-0.004}$	0.864 ± 0.008
T_{tot}	Total transit duration (h)	2.49 ± 0.01	2.54 ± 0.02
T_{full}	Full-transit duration (h)	$1.05^{+0.03}_{-0.04}$	$1.19^{+0.08}_{-0.07}$
$T_{0;\mathrm{occ}}$	Epoch occultation ($\mathrm{BJD_{TDB}}$)	$2458740.5013^{+0.0025}_{-0.0033}$	$2458740.5035^{+0.0043}_{-0.0031}$
b_{occ}	Impact parameter occultation	$0.87^{+0.02}_{-0.06}$	0.87 ± 0.02
$\rho_\star$	Host density from orbit ($\mathrm{g\,cm^{-3}}$)	$0.39^{+0.03}_{-0.02}$	0.40 ± 0.02
T_{eq} [a]	Equilibrium temperature (K)	2370 ± 70	2370 ± 70
$u_{1;\mathrm{TESS}}$	Limb darkening	$0.32^{+0.30}_{-0.20}$	$0.38^{+0.42}_{-0.26}$
$u_{2;\mathrm{TESS}}$	Limb darkening	$0.14^{+0.22}_{-0.29}$	$0.30^{+0.29}_{-0.45}$
$\delta_{\mathrm{tr;undil}}$	Transit depth (undil.) (ppt)	$5.829^{+0.008}_{-0.007}$	5.954 ± 0.010
$\delta_{\mathrm{tr;dil}}$	Transit depth (dil.) (ppt)	$5.800^{+0.008}_{-0.007}$	5.924 ± 0.010
$\delta_{\mathrm{occ;undil}}$	Occultation depth (undil.) (ppt)	0.124 ± 0.005	$0.147^{+0.007}_{-0.006}$
$\delta_{\mathrm{occ;dil}}$	Occultation depth (dil.) (ppt)	0.123 ± 0.005	$0.146^{+0.007}_{-0.006}$
$F_{\mathrm{night;undil}}$	Nightside flux (undil.) (ppt)	0.047 ± 0.005	$0.047^{+0.008}_{-0.007}$
$F_{\mathrm{night;dil}}$	Nightside flux (dil.) (ppt)	0.047 ± 0.005	$0.047^{+0.008}_{-0.007}$

[a] Calculated assuming zero Bond albedo.

star) with a depth of $\delta_{\mathrm{occ;dil}} = 0.124 \pm 0.005$ ppt. We also robustly detect the longitudinal modulation of the planet's light in the *TESS* band-pass ($A_{\mathrm{atmospheric}} = 0.077 \pm 008$ ppt) from the full phase curve, as shown in Figure 11, providing us with a rare opportunity to measure the planet's day/night brightness temperature contrast (see Section 5).

From the light curve, we see a very weak beaming signal with a measured amplitude of $A_{\mathrm{beaming}} = 0.0011^{+0.0016}_{-0.0007}$ ppt and a marginal detection of ellipsoidal modulation with an amplitude of $A_{\mathrm{ellipsoidal}} = 0.028 \pm 0.006$ ppt. The predicted full amplitudes of both of these phase curve components can be derived from theory and depend on the planet–star mass ratio $q_p = M_p/M_*$ (see, for example, the review in Shporer 2017):

$$A_{\mathrm{ellipsoidal}} = 2\alpha_{\mathrm{ellip}} q_p \left(\frac{R_*}{a}\right)^3 \sin^2 i_p, \tag{1}$$

$$A_{\mathrm{beaming}} = 2\left[\frac{2\pi G}{P_p c^3}\frac{q_p^2 M_p \sin^3 i_p}{(1+q_p)^2}\right]^{\frac{1}{3}} \left\langle \frac{xe^x}{e^x-1}\right\rangle_{\mathrm{TESS}}. \tag{2}$$

Here, we have assumed for simplicity that the stellar spectrum is a blackbody, and $x \equiv hc/k\lambda T_*$; the angled brackets indicate averaging over the *TESS* band-pass. The prefactor α_{ellip} in the ellipsoidal distortion is an expression that includes the limb- and gravity-darkening coefficients for the host star.

To calculate the predicted amplitudes, we use the stellar parameters derived from the SED fit (Table 1) and the best-fit system parameters from the joint transit and RV analysis (Section 4.2). For the limb- and gravity-darkening coefficients, we take tabulated values from Claret (2017) and interpolate to the measured stellar parameters. Uncertainties are propagated to the estimates using Monte Carlo sampling. We obtain predicted amplitudes of $A_{\mathrm{ellipsoidal}} = 0.028 \pm 0.004$ ppt and $A_{\mathrm{beaming}} = 0.0052 \pm 0.0004$ ppt. These theoretical values are in excellent agreement with our measured values to within the 1σ level.

Our phase-curve analysis did not consider a possible phase shift in the time of maximum brightness, which would correspond to an offset in the dayside hotspot. Previous studies of ultra-hot Jupiter have indicated very small (if any) phase-curve offsets (see, for example, the case of KELT-9 b; Wong et al. 2020b). Any offset would manifest itself in our phase-curve fits through its effect on the measured beaming amplitude. We have shown that the measured and predicted values of A_{beaming} are consistent to within 1σ. Therefore, we conclude that there is no evidence for a significant phase offset in the planet's atmospheric brightness modulation.

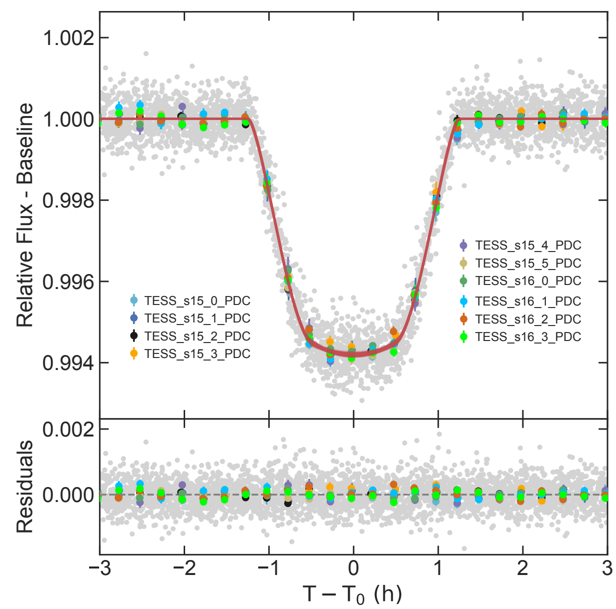

Figure 8. Phase-folded and detrended light curve of TOI-1431 from the simultaneous hybrid cubic spline detrending model, similar to Figure 7, but with the single-scale MAP corrected PDC data instead. The colored points represent the individual phased light curve segments across Sectors 15 and 16 that have been binned at a cadence of 15 m. The red solid lines are 20 light curve models drawn from the posteriors of the Nested Sampling analysis in `Allesfitter`.

4.1.3. *SAP Photometry*

We also performed the analysis of the pre-cleaned SAP light curve segments following the same procedures with the four different detrending techniques as done in Section 4.1.2. We then compared the results of the analysis of the SAP light curve with the results we obtained using the single-scale and multi-scale MAP corrected PDC light curves. The SAP light curve (see Figure 19 in the Appendix) also shows no evidence of the dip features near the transit.

We ran the Nested Sampling fits on the SAP light curve segments and compared the Bayesian evidence of the four detrending models, finding that the hybrid cubic spline detrending to be the most favored model. We then compared the fits of the single-scale MAP PDC light curve and the SAP light curve (with spline detrending) using the Bayes model comparison factor. The model that fit the single-scale MAP PDC light curve is decisively favored over the SAP light curve model, with a Bayes factor of $\ln R = 13432$. However, the results from the two models generally are in good agreement with each other to around the 1σ level with the exception of the transit (at $\sim 12\sigma$) and occultation depths ($\sim 3.3\sigma$)

as well as the amplitudes of the beaming ($\sim 1.8\sigma$) and atmospheric modulations ($\sim 2.3\sigma$) as given in Table 2).

In particular, the deeper transit depth measured with the SAP light curve compared to the single-scale MAP PDC light curve is likely the result of 'whisker'-like flux dips that are caused by brief spacecraft pointing excursions. These excursions result in the target pixel response function momentarily moving off center from the optimal aperture, causing slightly less flux to be measured for a fraction of a cadence that occasionally overlap with some of the transits (see Figure 1 and Figure 20 in the Appendix). While most of the 'whiskers' were removed in the SAP light curve (either from being quality flagged or from the median filter), the ones that occurred during a transit that were not quality flagged by the *TESS* pipeline, remained in the light curve, resulting in a deeper transit depth. The correction applied to the single-scale MAP PDC light curve from the use of the co-trending basis vectors has removed high frequency noise, including the 'whiskers' from the pointing shifts.

Despite the discrepancies in some parameters, the results for the planet radius, equilibrium temperature, and dayside and nightside brightness temperatures are still consistent within 1σ, due to the largest contributor to the uncertainties in these parameters being from the uncertainties in the stellar parameters. Therefore, the main conclusions of this paper do not change whether we use the results from the analysis of SAP or single-scale MAP PDC photometry. The introduced noise goodness metric for the single-scale PDC light curve gives an excellent score of 0.99941, which is indicative of little introduced noise. This combined with the Bayes model comparison factor strongly favoring the single-scale PDC light curve motivates our decision to prefer the PDC results.

4.2. *Joint Transit & Radial Velocity Analysis*

We perform a joint analysis in `Allesfitter` of the *TESS* single-scale MAP corrected PDC photometry, the high-quality photometric ground-based light curves from MuSCAT2 (four Sloan bands g', r', i', and z_s) taken on 16 May 2020 and LCOGT taken on 14 October 2020, and the radial velocity measurements obtained with the SONG, SOPHIE, FIES, NRES, and EXPRES instruments, to determine the planet properties and orbital parameters. The same uniform priors were applied on the model parameters that were applied from the single-scale MAP PDC light curve analysis in Section 4.1.2, but with optimized starting values from that analysis. Additionally, we performed the joint analysis using the *TESS* SAP photometry to compare the results from the analysis using the single-scale MAP PDC photometry. We also used the same Gaussian priors for the stellar parameters and *TESS* dilution parameter. Uniform priors with reasonable boundaries and starting values were also set for the parameters unique to the joint analysis, including the radial velocity semi-amplitude (K), set of limb-darkening coefficients (q_1 and q_2) for each of the ground-based light curves, flux error scaling ($\ln \sigma_{F_{inst}}$) for the ground-based light curves, and a radial velocity baseline offset (ΔRV_{inst}) and jitter term ($\log \sigma_{RV_{inst}}$) for each radial velocity instrument. Initially we used uniform priors on $\sqrt{e_p} \cos \omega_p$ and $\sqrt{e_p} \sin \omega_p$ but found no evidence of an eccentric orbit so fixed these parameters to 0 to improve performance.

For the joint analysis, we were not interested in fitting the full phase curve or occultation so the phase curve and surface brightness parameters are excluded. Instead, we chose the fast fit option for fitting the photometry, which masks the out-of-transit data to significantly improve fitting performance, using a width of 0.20 d (4.8 hr) centered around the midpoints of the transits. Similar to the stand-alone analysis of the *TESS* single-scale MAP PDC and SAP photometry, we applied the hybrid cubic spline detrending for each of the transit light curves used in the joint fit. The analysis was carried out using a MCMC that ran until it converged. We then ran a Nested Sampling fit using the best-fit MCMC values as starting values until the run reached the convergence criterion. Both the MCMC and Nested Sampling give consistent results, and we report the results of the Nested Sampling model in Table 3. In Figures 3 and 9, we show the radial velocity measurements and ground-based transit light curves with the corresponding models drawn from the Nested Sampling posterior, respectively.

Our preferred solution from the joint analysis using the single-scale MAP PDC light curve shows that TOI-1431 hosts a massive $3.14^{+0.19}_{-0.18}\,\mathrm{M_J}$ planet, and when combined with the measured radius, gives a mean density of $1.18^{+0.20}_{-0.17}\,\mathrm{g\,cm^{-3}}$, slightly less dense but consistent with the density of Jupiter ($1.326\,\mathrm{g\,cm^{-3}}$) and similar in density to other Jovian worlds. The large number and high quality of radial velocity measurements (as shown in Figure 3), coupled with the host star's low $v \sin i$ of $6.0 \pm 0.2\ \mathrm{km\,s^{-1}}$, has allowed us to measure the radial velocity semi-amplitude of the orbit ($294.1 \pm 1.1\ \mathrm{m\,s^{-1}}$) with unusually high precision for a planet orbiting such a hot star (7690^{+400}_{-250} K). In fact, this is the highest precision orbit measured for any planet that has a host star hotter than 6600 K. The largest contributor to the uncertainty in the planet mass (17.4σ detection) is from the uncertainty on the host star mass.

Table 3. Median values and 68% confidence interval of the fitted and derived parameters for TOI-1431b from the joint Nested Sampling **Allesfitter** analysis of the *TESS* single-scale MAP corrected PDC photometry, ground-based light curves, and radial velocity measurements. We also include the median values and 68% confidence interval of the same fitted and derived parameters from the joint analysis using the *TESS* SAP photometry instead as a comparison. †Preferred solution for the fitted and derived parameters.

Parameter	Description	Value (with PDC)†	Value (with SAP)
		Fitted parameters	
$R_b/R_\star$	Radius ratio	$0.0795^{+0.0008}_{-0.0006}$	$0.0805^{+0.0009}_{-0.0007}$
$(R_\star + R_b)/a$.	Radii sum to semi-major axis	0.2092 ± 0.0019	$0.2080^{+0.0024}_{-0.0025}$
$\cos i_b$	Cosine of inclination	0.171 ± 0.002	0.169 ± 0.003
T_0	Mid transit time ($\mathrm{BJD_{TDB}}$)	$2458739.17736 \pm 0.00008$	$2458739.17728 \pm 0.00011$
P_b	Orbital period (d)........................	2.650238 ± 0.000004	2.650241 ± 0.000004
K_b	RV semi-amplitude ($\mathrm{km\,s^{-1}}$)............	0.2941 ± 0.0011	0.2939 ± 0.0012
$D0_{\mathrm{TESS}}$	Dilution	0.0049 ± 0.0005	0.0049 ± 0.0005
$q1_{\mathrm{TESS}}$	Transformed limb darkening	0.20 ± 0.05	$0.33^{+0.08}_{-0.07}$
$q2_{\mathrm{TESS}}$	Transformed limb darkening	$0.17^{+0.18}_{-0.12}$	$0.17^{+0.17}_{-0.11}$
$q1_{\mathrm{LCOY}}$	Transformed limb darkening	$0.19^{+0.14}_{-0.10}$	$0.23^{+0.16}_{-0.12}$
$q2_{\mathrm{LCOY}}$	Transformed limb darkening	0.50 ± 0.30	$0.46^{+0.31}_{-0.28}$
$q1_{\mathrm{MuSCAT2z'}}$ ..	Transformed limb darkening	$0.25^{+0.12}_{-0.11}$	$0.34^{+0.15}_{-0.13}$
$q2_{\mathrm{MuSCAT2z'}}$ ..	Transformed limb darkening	$0.53^{+0.27}_{-0.29}$	$0.43^{+0.29}_{-0.26}$
$q1_{\mathrm{MuSCAT2r'}}$ ..	Transformed limb darkening	$0.40^{+0.14}_{-0.12}$	$0.50^{+0.15}_{-0.14}$
$q2_{\mathrm{MuSCAT2r'}}$ ..	Transformed limb darkening	$0.56^{+0.24}_{-0.26}$	0.47 ± 0.25
$q1_{\mathrm{MuSCAT2i'}}$ ...	Transformed limb darkening	$0.18^{+0.10}_{-0.08}$	$0.26^{+0.12}_{-0.10}$
$q2_{\mathrm{MuSCAT2i'}}$ ...	Transformed limb darkening	$0.61^{+0.25}_{-0.32}$	$0.56^{+0.26}_{-0.29}$
$q1_{\mathrm{MuSCAT2g'}}$ ..	Transformed limb darkening	$0.54^{+0.14}_{-0.12}$	$0.64^{+0.14}_{-0.13}$
$q2_{\mathrm{MuSCAT2g'}}$ ..	Transformed limb darkening	$0.64^{+0.20}_{-0.22}$	$0.63^{+0.20}_{-0.21}$
$\ln \sigma_{\mathrm{TESS}}$	Flux error scaling (ln rel.flux.)...........	-7.78 ± 0.01	-7.43 ± 0.01
$\ln \sigma_{\mathrm{LCOY}}$	Flux error scaling (ln rel.flux.)...........	-6.53 ± 0.04	-6.53 ± 0.04
$\ln \sigma_{\mathrm{MuSCAT2z'}}$	Flux error scaling (ln rel.flux.)...........	-6.92 ± 0.04	-6.92 ± 0.04
$\ln \sigma_{\mathrm{MuSCAT2r'}}$	Flux error scaling (ln rel.flux.)...........	-7.00 ± 0.04	-7.00 ± 0.05
$\ln \sigma_{\mathrm{MuSCAT2i'}}$	Flux error scaling (ln rel.flux.)...........	-7.03 ± 0.04	$-7.02^{+0.05}_{-0.04}$
$\ln \sigma_{\mathrm{MuSCAT2g'}}$	Flux error scaling (ln rel.flux.)...........	$-7.05^{+0.05}_{-0.04}$	-7.05 ± 0.05
$\log \sigma_{\mathrm{RV_{SONG}}}$.	RV jitter ($\mathrm{km\,s^{-1}}$)......................	$-7.5^{+1.8}_{-1.6}$	$-7.1^{+1.7}_{-1.8}$
$\log \sigma_{\mathrm{RV_{ELP}}}$ ...	RV jitter ($\mathrm{km\,s^{-1}}$)......................	$-2.9^{+0.4}_{-0.3}$	$-2.9^{+0.4}_{-0.3}$
$\log \sigma_{\mathrm{RV_{TLV}}}$ ...	RV jitter ($\mathrm{km\,s^{-1}}$)......................	$-2.8^{+0.2}_{-0.1}$	-2.8 ± 0.2
$\log \sigma_{\mathrm{RV_{FIES}}}$ ..	RV jitter ($\mathrm{km\,s^{-1}}$)......................	$-7.9^{+1.6}_{-1.3}$	-7.7 ± 1.5
$\log \sigma_{\mathrm{RV_{SOPHIE}}}$	RV jitter ($\mathrm{km\,s^{-1}}$)......................	$-5.9^{+1.0}_{-2.1}$	$-6.4^{+1.4}_{-2.3}$
$\log \sigma_{\mathrm{RV_{EXPRES}}}$	RV jitter ($\mathrm{km\,s^{-1}}$)......................	$-7.8^{+1.1}_{-1.4}$	$-7.8^{+1.2}_{-1.4}$
$\Delta \mathrm{RV_{SONG}}$ ...	RV offset ($\mathrm{km\,s^{-1}}$)......................	-25.154 ± 0.006	-25.154 ± 0.007
$\Delta \mathrm{RV_{ELP}}$	RV offset ($\mathrm{km\,s^{-1}}$)......................	$-25.578^{+0.022}_{-0.021}$	-25.577 ± 0.024

Table 3 *continued*

Table 3 *(continued)*

Parameter	Description	Value (with PDC)†	Value (with SAP)
ΔRV_{TLV}	RV offset ($km\,s^{-1}$)	-25.569 ± 0.012	-25.570 ± 0.012
ΔRV_{FIES}	RV offset ($km\,s^{-1}$)	-0.274 ± 0.002	-0.274 ± 0.002
ΔRV_{SOPHIE}	RV offset ($km\,s^{-1}$)	-25.249 ± 0.003	-25.249 ± 0.003
ΔRV_{EXPRES}	RV offset ($km\,s^{-1}$)	0.0049 ± 0.0007	0.0047 ± 0.0007
	Derived parameters		
$R_\star/a$	Host radius to semi-major axis	0.194 ± 0.002	0.193 ± 0.002
$a/R_\star$	Semi-major axis to host radius	5.16 ± 0.05	$5.19^{+0.07}_{-0.06}$
R_b	Planet radius ($R_\oplus$)	16.7 ± 0.6	16.9 ± 0.6
R_b	Planet radius (R_{jup})	1.49 ± 0.05	1.51 ± 0.06
a	Semi-major axis (AU)	0.046 ± 0.002	0.047 ± 0.002
i	Inclination (deg)	80.16 ± 0.14	$80.30^{+0.18}_{-0.17}$
b_{tra}	Impact parameter	0.882 ± 0.002	$0.875^{+0.005}_{-0.006}$
q_b	Mass ratio	0.00158 ± 0.00006	0.00157 ± 0.00006
M_b	Companion mass ($M_\oplus$)	1000 ± 60	990 ± 60
M_b	Companion mass (M_{jup})	$3.14^{+0.19}_{-0.18}$	$3.12^{+0.19}_{-0.18}$
T_{tot}	Total transit duration (h)	2.48 ± 0.01	2.51 ± 0.01
T_{full}	Full-transit duration (h)	1.04 ± 0.04	1.11 ± 0.05
$\rho_\star$	Host density from orbit (cgs)	0.37 ± 0.01	$0.38^{+0.02}_{-0.01}$
ρ_b	Companion density (cgs)	$1.18^{+0.20}_{-0.17}$	$1.13^{+0.19}_{-0.16}$
g_b	Companion surface gravity (cgs)	3450 ± 90	3400 ± 90
T_{eq}	Equilibrium temperature (K)	2390 ± 100	2390 ± 100
H_b	Companion atmospheric scale height (km)	220 ± 30	230 ± 30
$u_{1;TESS}$	Limb darkening	$0.16^{+0.17}_{-0.11}$	$0.20^{+0.19}_{-0.13}$
$u_{2;TESS}$	Limb darkening	$0.28^{+0.12}_{-0.16}$	$0.37^{+0.15}_{-0.19}$
$u_{1;LCOY}$	Limb darkening	$0.39^{+0.28}_{-0.24}$	$0.42^{+0.30}_{-0.25}$
$u_{2;LCOY}$	Limb darkening	$0.00^{+0.26}_{-0.23}$	$0.03^{+0.28}_{-0.26}$
$u_{1;MuSCAT2z'}$	Limb darkening	0.50 ± 0.27	$0.48^{+0.31}_{-0.28}$
$u_{2;MuSCAT2z'}$	Limb darkening	$-0.02^{+0.29}_{-0.24}$	0.08 ± 0.31
$u_{1;MuSCAT2r'}$	Limb darkening	$0.69^{+0.27}_{-0.31}$	$0.66^{+0.31}_{-0.34}$
$u_{2;MuSCAT2r'}$	Limb darkening	$-0.07^{+0.35}_{-0.28}$	$0.04^{+0.36}_{-0.33}$
$u_{1;MuSCAT2i'}$	Limb darkening	$0.49^{+0.25}_{-0.26}$	$0.55^{+0.27}_{-0.29}$
$u_{2;MuSCAT2i'}$	Limb darkening	$-0.09^{+0.26}_{-0.20}$	$-0.06^{+0.30}_{-0.24}$
$u_{1;MuSCAT2g'}$	Limb darkening	$0.92^{+0.25}_{-0.30}$	$0.96^{+0.26}_{-0.31}$
$u_{2;MuSCAT2g'}$	Limb darkening	$-0.20^{+0.33}_{-0.26}$	$-0.17^{+0.34}_{-0.28}$
$\delta_{TESS;undil}$	Transit depth (undil.) (ppt)	5.794 ± 0.008	$5.842^{+0.012}_{-0.011}$
$\delta_{TESS;dil}$	Transit depth (dil.) (ppt)	5.765 ± 0.008	$5.816^{+0.012}_{-0.011}$
δ_{LCOY}	Transit depth (ppt)	$5.67^{+0.26}_{-0.28}$	5.80 ± 0.27
$\delta_{MuSCAT2z'}$	Transit depth (ppt)	$5.55^{+0.23}_{-0.28}$	$5.64^{+0.23}_{-0.28}$
$\delta_{MuSCAT2r'}$	Transit depth (ppt)	$5.24^{+0.25}_{-0.28}$	$5.37^{+0.27}_{-0.28}$
$\delta_{MuSCAT2i'}$	Transit depth (ppt)	$5.63^{+0.25}_{-0.27}$	$5.69^{+0.22}_{-0.25}$
$\delta_{MuSCAT2g'}$	Transit depth (ppt)	$4.88^{+0.26}_{-0.27}$	4.96 ± 0.27

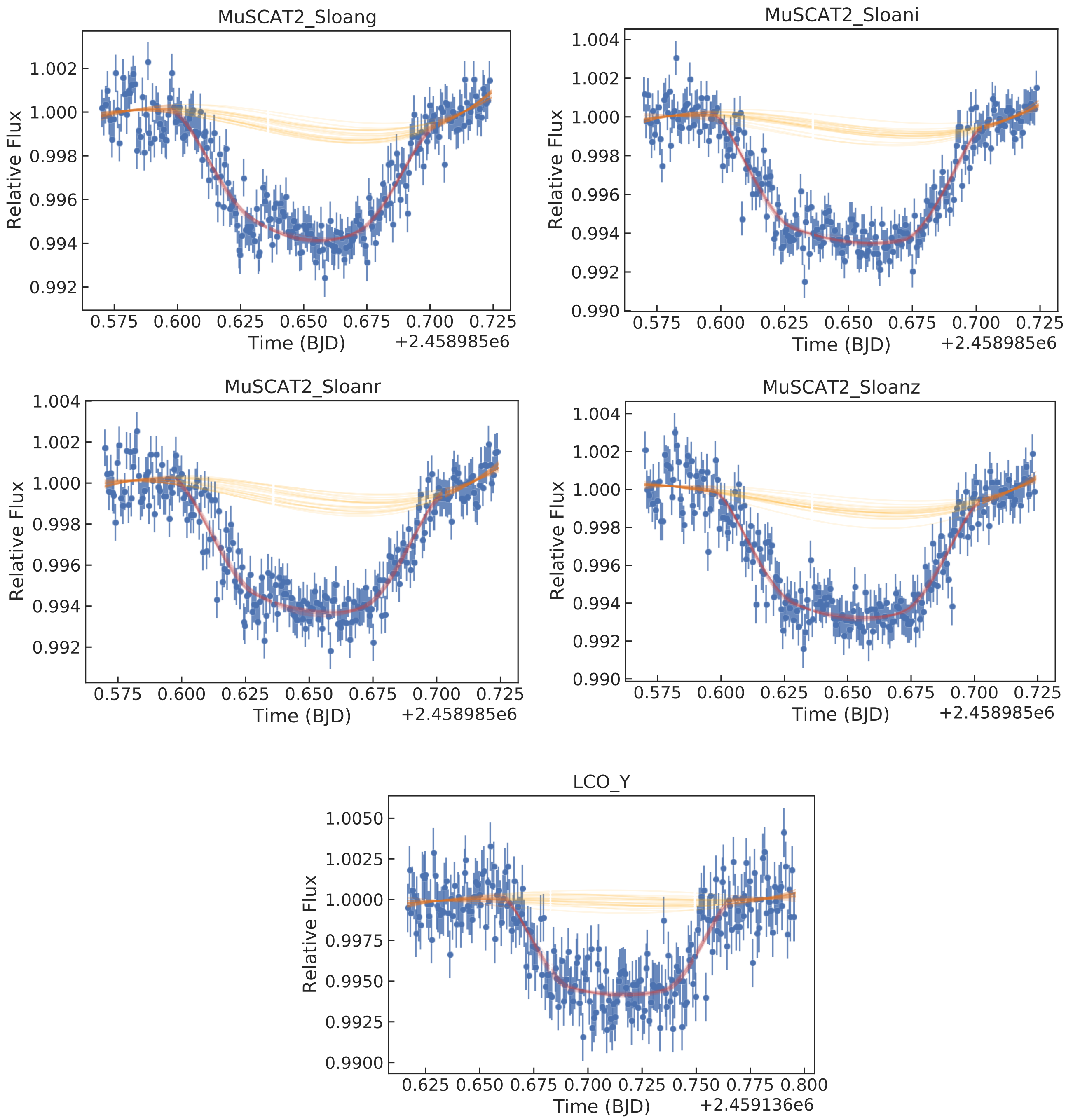

Figure 9. The ground-based transit light curves of TOI-1431 b/MASCARA-5 b as a function of time from the observations taken with the four MuSCAT2 photometric bands and from the LCO. The normalized photometric measurements are represented by the blue points, the 20 orange lines are the hybrid cubic spline detrending model drawn from random sampling of the posterior, and the transit light curve models are represented by the red lines and are also drawn from 20 random samples of the Nested Sampling posterior.

5. THE ATMOSPHERE

We have used the *TESS* single-scale MAP corrected PDC photometry and `Allesfitter` to characterize the red-optical (6000 − 9500 Å) phase curve of TOI-1431 b, which includes contributions from beaming, ellipsoidal modulation, and atmospheric brightness modulation, as well as the secondary eclipse (see Section 4.1.2). In Figure 11, the full phase curve is shown with the best-fit phase curve model components and the secondary eclipse light curve, which has a measured depth of $\delta_{\rm occ;dil} = 0.124 \pm 0.005$ ppt. We measured the amplitude of the atmospheric brightness modulation as $A_{\rm atm} = 0.077 \pm 0.008$ ppt. We also fit the phase curve and secondary eclipse using the *TESS* SAP photometry (see Figure 22 in the Appendix) as a comparison to our preferred solution using the single-scale MAP PDC photometry.

From the measured secondary eclipse depth $\delta_{\rm occ}$ and nightside planetary flux $\delta_{\rm night}$, we can derive the dayside and nightside brightness temperatures of TOI-1431 b using the relationship between the planet–star flux ratio δ, planetary emission $F_p(\lambda, T_p)$ (assumed to be a blackbody), and stellar spectrum $F_*(\lambda, T_{\rm eff})$:

$$\delta = \left(\frac{R_p}{R_*}\right)^2 \frac{\int F_p(\lambda, T_p)\tau(\lambda)d\lambda}{\int F_*(\lambda, T_{\rm eff})\tau(\lambda)d\lambda} + A_g\left(\frac{R_p}{a}\right)^2. \quad (3)$$

Any reflected light on the dayside atmosphere contributes to the measured flux ratio through the geometric albedo A_g; this second term is zero when computing the nightside temperature. The planetary and stellar spectra are integrated over the *TESS* band-pass, which has a transmission function (in energy units) represented by $\tau(\lambda)$.

We model the star's spectrum using PHOENIX models (Husser et al. 2013). To properly interpolate the stellar models and propagate the uncertainties in stellar parameters to the planetary temperature estimates, we follow the methodology described in Wong et al. (2020b) and calculate the integrated stellar flux within the *TESS* band-pass for a grid of PHOENIX models, before fitting a cubic polynomial in $(T_{\rm eff}, \log g, [{\rm Fe/H}])$ to the full set of values. We then use a standard MCMC routine to compute the posterior distribution of the planetary brightness temperature T_p, with Gaussian priors on the stellar and system parameters, as well as the measured dayside or nightside flux ($\delta_{\rm occ}$ or $\delta_{\rm night}$; see Table 2).

For the dayside brightness temperature, we obtain $T_{\rm day} = 2983^{+63}_{-68}$ K when assuming zero geometric albedo; across an albedo range of 0–0.2, we find dayside brightness temperatures spanning 2800–3100 K. We measure a very high nightside brightness temperature of $T_{\rm night} = 2556^{+62}_{-65}$ K. The extremely hot dayside is expected to preclude the formation of condensates, resulting in a cloudfree dayside hemisphere (e.g., Wakeford et al. 2017). Previous analyses of other ultra-hot Jupiters combining secondary eclipses at optical and thermal infrared wavelengths confirm the predictions of low reflectivity, yielding near-zero geometric albedos (e.g., WASP-18b and WASP-33b; Shporer et al. 2019; von Essen et al. 2020).

We use the measured dayside and nightside brightness temperatures to jointly constrain the Bond albedo $A_{\rm B}$ and the efficiency of heat recirculation from the dayside to nightside of the planet ϵ (0 for no recirculation; 1 for full recirculation), following the thermal balance formalism outlined in Cowan & Agol (2011) and the methodology described in Wong et al. (2020b). We find $A_B = -0.84^{+0.30}_{-0.39}$ and $\epsilon = 0.76 \pm 0.05$. The very efficient day-night heat recirculation is borne out by the low day/night temperature contrast (∼400 K). However, the unusual negative Bond albedo suggests that the overall thermal emission level across the entire planet cannot be accounted for by the energy input from stellar insolation alone.

By placing TOI-1431 b in context, we can appreciate the exceptional atmospheric properties of this planet. Figure 10 shows the nightside brightness temperatures, Bond albedos, and recirculation efficiencies for a sample of hot and ultra-hot Jupiters, taken and/or analogously derived from the brightness temperatures listed in the comprehensive Spitzer 4.5 μm phase curve analysis by Bell et al. (2020). From the plots, it is evident that TOI-1431 b has a much higher nightside temperature and day-night heat recirculation efficiency than most other hot Jupiters with comparable equilibrium temperatures. Meanwhile, only HAT-P-7 b has a similar strongly ($> 2\sigma$) negative inferred Bond albedo; indeed, HAT-P-7 b is very similar to TOI-1431 b in all respects. Broadly speaking, both HAT-P-7 b and TOI-1431 b are outliers amid the weak overall trends across gas giants with $1200 < T_{\rm eq} < 3000$ K, i.e., increasing nightside temperature, decreasing Bond albedo, and decreasing day-night heat recirculation efficiency with increasing equilibrium temperature.

The unexpected negative Bond albedo may indicate the limitations of the simple thermal balance considerations underpinning our estimates of A_B and ϵ. In particular, gradients in chemical composition between the dayside and nightside hemispheres can entail drastically different atmospheric opacities, meaning that the pressure levels probed by our broadband photometric measurements may vary significantly across the planet's surface. Another explanation for a negative Bond albedo is additional thermal emission from residual heat of for-

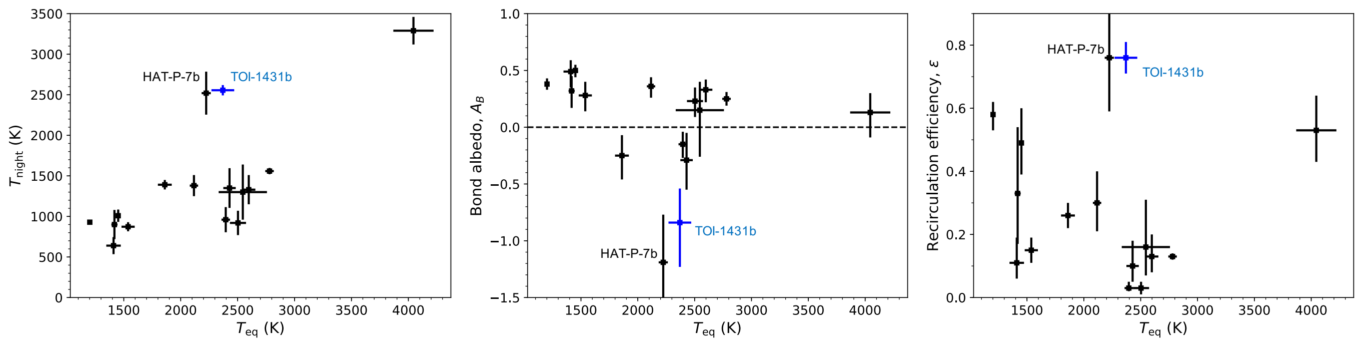

Figure 10. Plots of nightside brightness temperature $T_{\rm night}$, Bond albedo A_B, and day-night heat recirculation efficiency ϵ as a function of equilibrium temperature $T_{\rm eq}$ for a population of hot and ultra-hot Jupiters. TOI-1431 b is indicated in blue; the black points are taken/derived from the results of Bell et al. (2020). KELT-16b has been omitted due to its very large nightside temperature uncertainty (> 400 K) and poorly constrained ϵ value. With its high nightside temperature, low day/night temperature contrast, and strongly negative Bond albedo, TOI-1431 b is a notable outlier among gas giants with similar levels of stellar irradiation, and is very similar to HAT-P-7b.

mation. This scenario would increase the emitted flux at all longitudes, raising the measured brightness temperatures on both the dayside and the nightside hemispheres.

This explanation may be especially applicable to TOI-1431 b: the stellar age inferred from SED modeling is $0.29^{+0.32}_{-0.19}$ Gyr, making the system among the youngest giant planet hosting systems hitherto discovered. However, the age of the planet is sufficient for it to have deflated through the initial Kelvin-Helmholtz contraction phase and for its atmosphere to have cooled and reached the equilibrium temperature. The time scale over which this initial cooling and deflation occurred is ~ 1 Myr (see Equation 17 from Ginzburg & Sari 2015), the photospheric cooling time to reach the regime where stellar irradiation acts to slow cooling. The current level of incident stellar flux is sufficient to slow the planet's interior cooling and allow it to remain hot and inflated at its present-day radius (see Figure 21 in the Appendix and Komacek et al. 2020). We do not require deposited heating in the deep interior to explain the present-day radius, however, a weak conversion of $\lesssim 0.07\%$ of the incident stellar flux to deposited heating is allowed. Importantly, we find that the effects of irradiation slowing cooling can only explain the present-day radius if TOI-1431 b arrived at its current orbit within ~ 1 Myr after formation. This may imply that TOI-1431 b either formed in-situ or that a nearby stellar or massive planetary companion rapidly scattered the planet inward very soon after formation. The high obliquity orbit as measured by the Rossiter-McLaughlin effect (Stangret et al., under review, see Section 6.2), suggests that the planet experienced just such a scattering event early in its history.

Future spectrally-resolved emission spectra with the James Webb Space Telescope (JWST) can enable detailed analyses of the atmospheric composition and temperature–pressure profiles across the planet's surface, providing a full picture of the thermal energy budget for TOI-1431 b.

From the derived equilibrium temperature and surface gravity of the planet and assuming a H/He atmosphere with a mean molecular mass of $\mu = 2.3$ amu, the calculated atmospheric scale height (from $H_{\rm p} = kT_{eq}/(\mu g_{\rm p})$) is $H_{\rm p} = 220 \pm 30$ km. While not the largest scale height among the population of hot Jupiters, this planet orbits one of the brightest host stars ($J_{mag} = 7.541 \pm 0.030$ and $K_{mag} = 7.439 \pm 0.030$, see Figure 12) making it a potential target for future atmospheric characterization through transmission spectroscopy.

The transmission spectroscopy metric (TSM, see, Kempton et al. 2018), used to assess the suitability of transmission spectroscopy observations with JWST, is ~ 110 for TOI-1431 b. Planets with TSM values greater than 90 (for Jovians and sub-Jovians), such as for this planet, are considered suitable for these observations with JWST. However, transmission spectroscopy carried out by Stangret et al. (under review) from two HARPS-N and one EXPRES transit observations finds no absorption signatures in the planet's atmosphere, likely due to its high surface gravity. Additionally, given the detection of the phase curve and secondary eclipse in the *TESS* red-optical band photometry, this will be an excellent target for emission spectroscopy with JWST. In particular, phase curve observations carried out with the Near Infrared Imager and Slitless Spectrograph (NIRISS) over wavelengths between 0.6 and 5.0 μm should provide a high-precision global temperature map of this planet's atmosphere (Parmentier & Crossfield 2018). Measurements of the abundances of molecular species as a function of longitude (chemical mapping) could also be probed through phase-resolved spectroscopic observations taken with JWST's NIRCam and NIRSpec instruments.

TOI-1431 b will also be a great target for detailed atmospheric characterization by the European Space Agency's *Atmospheric Remote-sensing Infrared Exoplanet Large-survey* (ARIEL, Tinetti et al. 2018) telescope. ARIEL will operate in the infrared with a spectral range between 1.25–7.8 μm as well as multiple narrow-band photometry in the optical. As such, it will be well suited to potentially measure this planet's equilibrium chemistry, trace gases, vertical and horizontal thermal structures, and the detection of clouds and cloud composition (assuming the atmosphere is not cloud free) through transmission and emission spectroscopy and phase curve observations.

6. DISCUSSION

TOI-1431 b joins the growing list of $\sim$ 16 hot and ultra-hot Jovians with measured full phase curves and secondary eclipses. With a dayside and nightside brigntness temperatures of $T_{\rm day} = 2983^{+63}_{-68}$ K and $T_{\rm night} = 2556^{+62}_{-65}$ K, respectively, TOI-1431 b is one of the hottest known exoplanets.

We have measured the mass of TOI-1431 b to be $M_{\rm p} = 3.14^{+0.19}_{-0.18}\,{\rm M_J}$ from radial velocity observations obtained from the SONG, SOPHIE, FIES, NRES TLV and ELP, and EXPRES spectrographs. When combined with the planet radius of $R_{\rm p} = 1.51 \pm 0.06\,{\rm R_J}$, this mass gives a bulk density of $\rho_{\rm p} = 1.18^{+0.20}_{-0.17}\,{\rm g\,cm^{-3}}$, similar to Jupiter ($1.326\,{\rm g\,cm^{-3}}$). The measured radial velocity semi-amplitude of $K = 294.1 \pm 1.1\,{\rm m\,s^{-1}}$ is the most precise K measurement for a planet-hosting star hotter than 6600 K. A large contributing factor for this is the unusually slow projected stellar rotational velocity of $v \sin i < 10\,{\rm km\,s^{-1}}$.

Figure 13 shows a plot of the planet radius as a function of planet mass while Figure 14 is a plot of planet radius as a function of stellar irradiation for all known Jovians and sub-Jovians with measured masses and radii. The radius of TOI-1431 b is inflated compared to other exoplanets of similar mass as shown in Figure 13, but is not so inflated when accounting for the very high insolation flux ($5300^{+500}_{-470}{\rm S_\oplus}$, see Figure 14), indicating that the planet inflation is likely the result of stellar irradiation and youthful age ($0.29^{+0.32}_{-0.19}$ Gyr).

6.1. *Metal Peculiar Am Star*

TOI-1431 b orbits a bright ($V_T \sim 8.0$ and $J \sim 7.5$) and very hot ($T_{\rm eff} \sim 7700$ K) host star. In fact, TOI-1431 is one of the hottest planet hosting stars as shown in Figure 15. The star is also classified as being a non-magnetic metallic-line chemically peculiar Am star (see, Conti 1970; Figueras et al. 1991; Renson et al. 1991). Am stars typically have slow rotation rates compared to typical 'field' A stars of similar effective temperatures (A star $v \sin i$ range between ~ 100 to $\sim 150\,{\rm km\,s^{-1}}$, see for example, Abt & Morrell 1995), which is certainly the case for TOI-1431 (assuming the star is not being observed nearly pole-on). The slow rotation of these stars is believed to be due to a close orbiting ($2.5 \lesssim P \lesssim 100$ d) stellar companion (Am stars are often found to be binary systems, see, Böhm-Vitense 2006) that raises tidal forces on the primary star, causing the primary to lose angular momentum and spin down (Michaud et al. 1983).

This in turn results in the onset of gravitational settling and radiative levitation due to the lack of mixing in the shallow convective envelopes of slow rotating A stars that produces a chemical peculiarity observed as a photospheric overabundance of iron-peak elements (such as Cr, Mn, Fe, and Ni and specifically of Ba, Y and Sr) but depleted abundances of light elements such as Ca, Sc and Mg (e.g., see, Preston 1974; Michaud et al. 1983; Charbonneau 1993; Böhm-Vitense 2006; Xiang et al. 2020).

The spectroscopic analysis of TOI-1431 from spectra collected from SONG reveals that the star has an overall metallicity slightly lower than the Solar abundance ([M/H] $= -0.15 \pm 0.10$ dex) and even less so in alpha elements (such as O, Mg, Si, S, Ca, and Ti) with $[\alpha/{\rm H}] = -0.27 \pm 0.10$ dex, while analysis of the SOPHIE spectra gives a somewhat higher than Solar abundance of iron ([Fe/H] $= 0.09 \pm 0.03$). This seems to suggest that the star has an overabundance of iron group elements and an under-abundance of light elements (compared with normal A stars) that is characteristic of Am stars. However, a more detailed analysis of the stellar spectra is required to confirm the Am star classification.

Another interesting feature of Am stars is the "anomalous luminosity effect", which causes deviations in the strengths of specific spectral lines from what is expected from normal main-sequence A stars at a given effective temperature (Bolton 1971). This means that depending on the spectral lines used when fitting the stellar spectrum model, one can obtain very different values for a star's effective temperature and surface gravity, hence the overall stellar classification. This appears to be the case for TOI-1431 (especially for $\log g$); the analysis of SONG spectra gives a $T_{\rm eff} = 6764 \pm 120$ K and $\log g = 2.76 \pm 0.26$ dex, the FIES spectral analysis gives $T_{\rm eff} = 6910 \pm 50$ K and $\log g = 3.29 \pm 0.10$ dex, and the SOPHIE spectral analysis gives $T_{\rm eff} = 6950 \pm 60$ K and $\log g = 4.72 \pm 0.08$ dex.

Planets orbiting main-sequence Am stars appear to be quite rare–only six that transit have been discov-

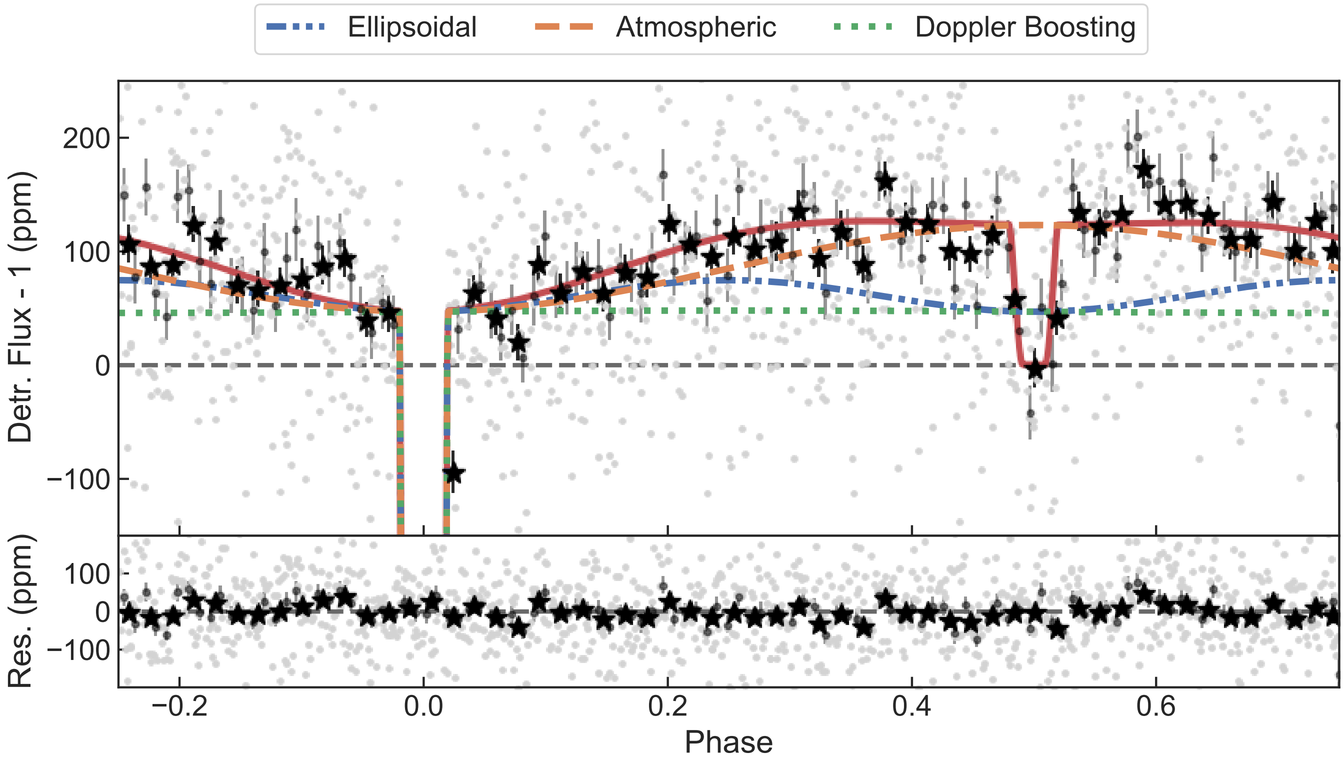

Figure 11. The phase-folded *TESS* single-scale MAP PDC light curve for TOI-1431 b, zoomed in to show the phase curve and secondary eclipse. The grey points are the detrended photometry, the dark grey points are the binned photometry with a cadence of $P_p/300$ ($\sim$ 12.7 m), and the black stars are the binned photometry with a cadence of $P_p/150$ ($\sim$ 25.5 m). Included in the phase curve model fit are the ellipsoidal (blue dash-dotted line), the atmospheric (orange dashed line), and the beaming modulations (green dotted line). The combined median model fit is plotted as the solid red line. The dark grey dashed line represents no emission from TOI-1431 b. The bottom panel shows the residuals to the combined median model.

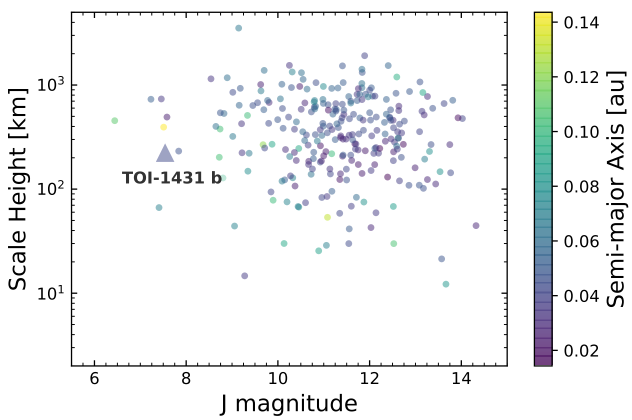

Figure 12. The atmospheric scale heights of hot Jupiters as a function of host star brightness in the Jmag. The points are colored based on the distance from the host star, with TOI-1431 b plotted as a triangle. This planet transits one of the brightest stars, making it an excellent candidate for future follow-up atmospheric studies.

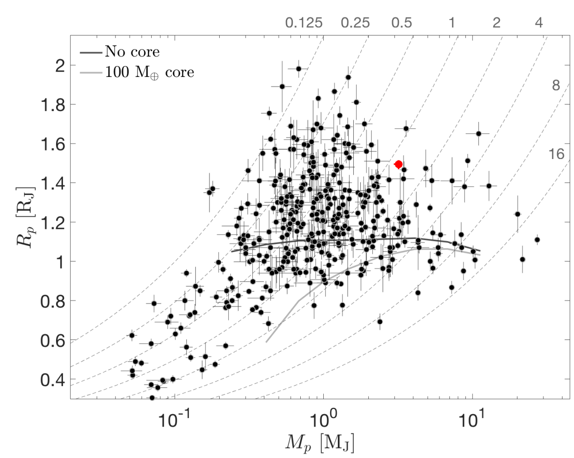

Figure 13. Planet mass versus radius of hot Jupiters. The red point is the location of TOI-1431 b. Planets located above the dark grey solid line are predicted to have no solid core while those plotted below the light grey solid line are predicted to have a solid core of at least 100 $M_\oplus$ (Fortney et al. 2007). The dotted lines are isodensity lines, with the density value given in the top-left, in cgs units. This plot shows that TOI-1431 b is moderately inflated compared to other Jovians of similar mass.

ered to date and these include TOI-1431 b, WASP-33 b (Collier Cameron et al. 2010b), KELT-17 b (Zhou et al. 2016c; Saffe et al. 2020, 2021), KELT-19A b (Siverd

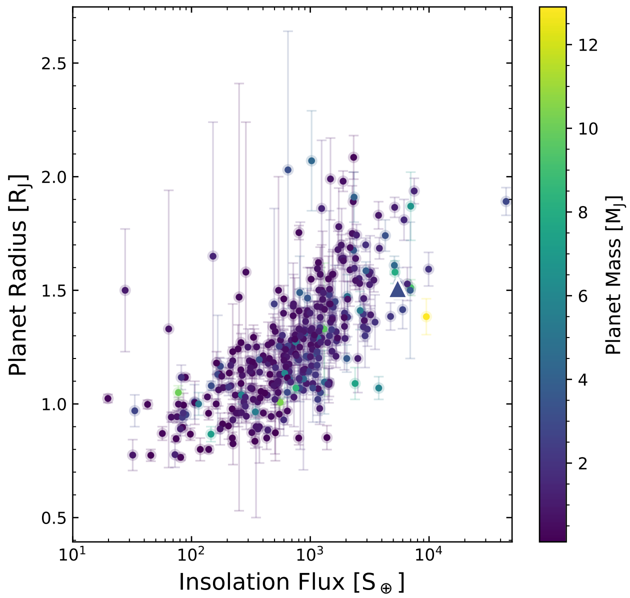

Figure 14. Incident stellar irradiation versus planet radius for all known Jovians and sub-Jovians that have measured masses and radii with the planet masses indicated by the color scale on the left. TOI-1431 b is plotted as the colored triangle on the right and it is clear that this planet is one of the most highly irradiated planets.

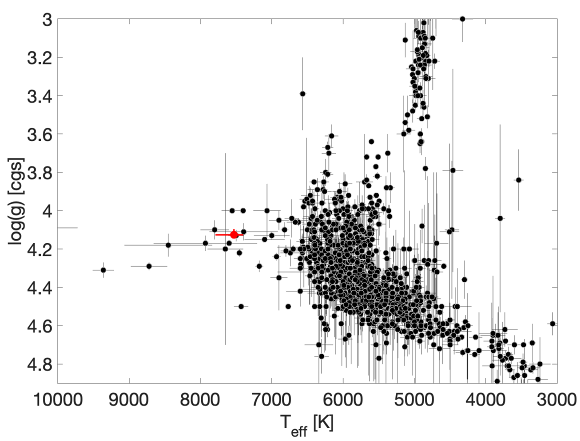

Figure 15. Plot of stellar effective temperature versus surface gravity for planet hosting stars. TOI-1431 is plotted as the red point and shows that it is one of the hottest (top 1%) known planet hosting stars.

et al. 2018c), WASP-178 b (Hellier et al. 2019), and KELT-26 b (Rodríguez Martínez et al. 2020). This raises some interesting questions. First, what is the occurrence rate of planets around Am stars? Radial velocity surveys have historically avoided hot and early type stars ($T_{\rm eff} > 6500$ K and mid-F and earlier), instead have targeted 'Solar analogs' (i.e., late-F, G, and K type stars, see, Cumming et al. 1999; Tinney et al. 2001b; Pepe et al. 2004; Valenti & Fischer 2005; Wright et al. 2008) in the search for planets. As such, planets orbiting hot main-sequence A stars like TOI-1431 have gone nearly undiscovered, until now thanks to *TESS* indiscriminately surveying the sky for transiting planets orbiting bright stars. Planets have been discovered orbiting former A stars, i.e., stars that have evolved off the main-sequence to become giant and sub-giant stars, in radial velocity surveys targeting such stars (e.g. Johnson et al. 2006; Trifonov et al. 2014; Reffert et al. 2015b; Jones et al. 2016; Luhn et al. 2019; Wittenmyer et al. 2020). Recent results from surveys of evolved stars indicate that the occurrence rate of giant planets around giant stars is ∼10 percent (e.g., Wittenmyer et al. 2020; Wolthoff et al., under review), indicating that giant planets are relatively common around hot stars and could also be common around Am stars as well.

If giant planet formation around A-type stars is indeed a relatively common occurrence, could the migration of a Jovian planet to a close-in orbit around its host (as presumed to be the case for TOI-1431 b) play a significant role in its tidal spin-down and as such, contribute to its nature as being an Am star? For TOI-1431 b, we do not see any conclusive evidence for this given that the system does not appear to be tidally synchronized ($P_{\rm p} \simeq P_{\rm rot}$) based on the host star's rotation period of between ~ 10 to ~ 16 d (from spectroscopic measurements of $v \sin i$) and the planet's orbital period of ~ 2.65 d. However, the one caveat is that the orientation of the stellar spin axis ($I_\star$) is unknown and the star could perhaps be spinning more rapidly if we are observing it nearly pole-on (leaving open the possibility of $P_{\rm p} \simeq P_{\rm rot}$). If indeed giant planets can contribute to the nature of their host's being an Am star, for Am stars without evidence of a stellar binary, do most or all have hot Jupiters? Radial velocity and transit searches targeting Am stars could resolve this question as well as provide valuable insights into the formation and evolution of Am stars, a process that is not fully understood.

6.2. *Projected Spin-Orbit Angle*

We attempted to measure the projected spin-orbit alignment (λ) of this system, using the planetary shadow technique (e.g., see, Collier Cameron et al. 2010a; Johnson et al. 2014; Zhou et al. 2016a), by acquiring in-transit high-resolution spectroscopic observations with the FIES instrument. We observed a transit of TOI-1431 b on the night of 23 May 2020 using FIES, obtaining a total of 30 exposures, each with an exposure time of 300 s and with airmass decreasing from 1.88 to 1.16 throughout the observation. The wavelength calibrated 2-D reduced spectra were extracted as outlined in Section 2.3.3. We then followed a procedure similar to that of Hoeijmakers et al. (2020) to attempt to extract the absorption line deformations during the transit of the planet. This involved first cross-correlating a continuum-normalized model template of the stellar spectrum of TOI-1431 with the telluric-corrected FIES spectra (in the stellar rest frame) to produce in-transit cross-correlation functions (CCFs). The in-transit CCFs were then divided by the mean out-of-transit CCF to retrieve the Doppler shadow map as shown in Figure 16.

From our analysis, the planetary shadow is not clearly detected from the FIES data, likely because of the slow rotation of the star. However, observations taken with HARPS-N and EXPRES of three transits of TOI-1431 b do successfully detect the Rossiter-McLaughlin effect, revealing that the planet is on a retrograde orbit with $\lambda = -155.3^{+16.1}_{-11.3}$ deg (Stangret et al., under review). The results of Stangret et al. (under review) suggest that TOI-1431 b likely experienced high-eccentricity migration in the past that produced its high obliquity orbit and then later the orbit was tidally circularized to the ~ 2.65 day period we observe today (for dissenting views of the formation of close-in gas giant planets in-situ via the core-accretion process and spin-orbit misalignments due to processes unrelated to planet migration, see e.g., Batygin et al. 2016; Hasegawa et al. 2019; Louden et al. 2021; Hjorth et al. 2021). This result follows the general pattern observed by other studies that the hottest stars tend to host planets on misaligned orbits (e.g., Winn et al. 2009; Albrecht et al. 2012; Louden et al. 2021).

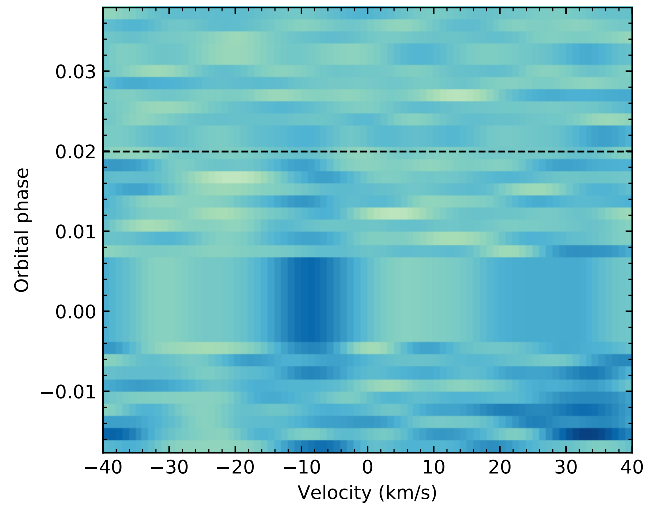

Figure 16. The spectroscopic stellar line profile map of TOI-1431 taken with FIES during and after the transit of TOI-1431 b in an attempt to observe the Doppler shadow cast by the planet. The dashed line indicates the end of the transit. There is a gap in the data around the middle of the transit (in the diagram, this region takes the values from the last CCF before the data gap). If the planet signal was strong enough to be detected, it would appear as a dark blue trail in the line profile residuals between ingress and egress. No clear signal is present in the data indicating that we are not able to detect the Doppler shadow of the planet and measure its spin-orbit alignment.

7. CONCLUSIONS

We have presented the discovery of the transiting ultra-hot Jupiter, TOI-1431 b. This planet orbits one of the hottest ($T_{\rm eff} = 7690^{+400}_{-250}$ K) and brightest ($V_T \sim 8.0$) of the known host stars with a period of just $P_p = 2.65022 \pm 0.00001$ d, resulting in it receiving a high amount of insolation flux and being moderately inflated. A joint analysis of the *TESS* light curve, ground-based light curves from MuSCAT2 and LCOGT, and radial velocities from SONG, SOPHIE, FIES, NRES, and EXPRES instruments results in a planet radius of $R_p = 1.51 \pm 0.06\,{\rm R_J}$ ($16.9^{+0.7}_{-0.6}\,{\rm R_\oplus}$) and a planet mass of $3.14^{+0.19}_{-0.18}\,{\rm M_J}$, corresponding to a bulk density of $1.18^{+0.20}_{-0.17}\,{\rm g\,cm^{-3}}$.

The planet's phase curve and secondary eclipse have been detected from the *TESS* photometry, providing us with the exciting opportunity to measure the planet's dayside and nightside temperatures as $T_{\rm day} = 2983^{+63}_{-68}$ K and $T_{\rm night} = 2556^{+62}_{-65}$ K, respectively, when assuming zero dayside geometric albedo. Among the population of hot/ultra-hot Jupiters, TOI-1431 b has the second highest measured nightside temperature and day-night heat recirculation efficiency.

It is also an excellent candidate for future follow-up observations with JWST and ARIEL to measure its transmission and emission spectra as well as obtain a high-precision global temperature and cloud map of this planet's atmosphere. Furthermore, the discovery and characterization of planets orbiting Am stars, for which few planets have been found, provides good opportunities to probe the tidal interactions between Jovian planets and hot host stars and the potential mechanisms responsible for the creation and evolution of Am stars.

ACKNOWLEDGMENTS

Based on observations made with the Hertzsprung SONG telescope operated on the Spanish Observatorio del Teide on the island of Tenerife by the Aarhus and Copenhagen Universities and by the Instituto de Astrofísica de Canarias.

Funding for the Stellar Astrophysics Centre is provided by The Danish National Research Foundation (Grant agreement no.: DNRF106).

Based on observations made with the Nordic Optical Telescope, operated by the Nordic Optical Telescope

Scientific Association at the Observatorio del Roque de los Muchachos, La Palma, Spain, of the Instituto de Astrofisica de Canarias under programs 59-210, 59-503, and 61-804.

Based on observations collected with the SOPHIE spectrograph on the 1.93 m telescope at the Observatoire de Haute-Provence (CNRS), France.

This article is based on observations made with the MuSCAT2 instrument, developed by ABC, at Telescopio Carlos Sánchez operated on the island of Tenerife by the IAC in the Spanish Observatorio del Teide.

This work makes use of observations from the LCOGT network. LCOGT telescope time was granted by NOIRLab through the Mid-Scale Innovations Program (MSIP). MSIP is funded by NSF.

B.A. is supported by Australian Research Council Discovery Grant DP180100972. The SONG telescope network is partially supported by the Australian Research Council Linkage, Infrastructure, Equipment and Facilities grant LE190100036.

V.A. was supported by a research grant (00028173) from VILLUM FONDEN.

I.W. is supported by a Heising-Simons *51 Pegasi b* postdoctoral fellowship.

Funding for the TESS mission is provided by NASA's Science Mission directorate. We acknowledge the use of public TESS Alert data from pipelines at the TESS Science Office and at the TESS Science Processing Operations Center. This research has made use of the Exoplanet Follow-up Observation Program website, which is operated by the California Institute of Technology, under contract with the National Aeronautics and Space Administration under the Exoplanet Exploration Program. Resources supporting this work were provided by the NASA High-End Computing (HEC) Program through the NASA Advanced Supercomputing (NAS) Division at Ames Research Center for the production of the SPOC data products. This paper includes data collected by the TESS mission, which are publicly available from the Mikulski Archive for Space Telescopes (MAST). This paper is partially based on observations made with the Nordic Optical Telescope, operated by the Nordic Optical Telescope Scientific Association at the Observatorio del Roque de los Muchachos, La Palma, Spain, of the Instituto de Astrofisica de Canarias.

TD acknowledges support from MIT's Kavli Institute as a Kavli postdoctoral fellow.

M.Y. and H.V.S. acknowledge the support by the research fund of Ankara University (BAP) through the project 18A0759001.

This work was supported by Fundação para a Ciência e a Tecnologia (FCT) and Fundo Europeu de Desenvolvimento Regional (FEDER) via COMPETE2020 through the research grants UIDB/04434/2020, UIDP/04434/2020, PTDC/FIS-AST/32113/2017 & POCI-01-0145-FEDER-032113, PTDC/FIS-AST/28953/2017 & POCI-01-0145-FEDER-028953.

O.D.S.D. is supported in the form of work contract (DL 57/2016/CP1364/CT0004) funded by FCT.

This work was supported by FCT - Fundação para a Ciência e a Tecnologia through national funds and by FEDER through COMPETE2020 - Programa Operacional Competitividade e Internacionalização by these grants: UID/FIS/04434/2019; UIDB/04434/2020; UIDP/04434/2020; PTDC/FIS-AST/32113/2017 & POCI-01-0145-FEDER-032113; PTDC/FIS-AST/28953/2017 & POCI-01-0145-FEDER-028953; PTDC/FIS-AST/28987/2017 & POCI-01-0145-FEDER-028987.

SH acknowledges CNES funding through the grant 837319

G.H. and I.B. received funding from the French Programme National de Planétologie (PNP) of CNRS (INSU).

This work is partly supported by JSPS KAKENHI Grant Numbers JP18H01265 and JP18H05439, and JST PRESTO Grant Number JPMJPR1775, and a University Research Support Grant from the National Astronomical Observatory of Japan (NAOJ).

M.N.G. acknowledges support from MIT's Kavli Institute as a Juan Carlos Torres Fellow.

T.D.K. acknowledges support from the 51 Pegasi b Fellowship in Planetary Astronomy sponsored by the Heising–Simons Foundation.

Facilities: TESS, SONG, SOPHIE, NRES ELP, NRES TLV, FIES, EXPRES, LCOGT, MuSCAT2, MASCARA

Software: AstroImageJ (Collins et al. 2017), TAPIR (Jensen 2013), `Allesfitter` (Günther & Daylan 2020, 2019), EXOFASTv2 (Eastman et al. 2013; Eastman 2017; Eastman et al. 2019), Astropy (Astropy Collaboration et al. 2018), Matplotlib (Hunter 2007)

REFERENCES

Abt, H. A., & Morrell, N. I. 1995, ApJS, 99, 135, doi: 10.1086/192182

Addison, B. C., Tinney, C. G., Wright, D. J., et al. 2013, ApJL, 774, L9, doi: 10.1088/2041-8205/774/1/L9

Addison, B. C., Wright, D. J., Nicholson, B. A., et al. 2020, MNRAS, doi: 10.1093/mnras/staa3960

Albrecht, S., Winn, J. N., Butler, R. P., et al. 2012, ApJ, 744, 189, doi: 10.1088/0004-637X/744/2/189

Alibert, Y., Mordasini, C., Benz, W., & Winisdoerffer, C. 2005, A&A, 434, 343, doi: 10.1051/0004-6361:20042032

Andersen, M. F., Grundahl, F., Christensen-Dalsgaard, J., et al. 2014, in Revista Mexicana de Astronomia y Astrofisica Conference Series, Vol. 45, Revista Mexicana de Astronomia y Astrofisica Conference Series, 83. https://arxiv.org/abs/1901.08300

Antoci, V., Handler, G., Grundahl, F., et al. 2013, MNRAS, 435, 1563, doi: 10.1093/mnras/stt1397

Asplund, M., Grevesse, N., Sauval, A. J., & Scott, P. 2009, ARA&A, 47, 481, doi: 10.1146/annurev.astro.46.060407.145222

Astropy Collaboration, Price-Whelan, A. M., Sipőcz, B. M., et al. 2018, AJ, 156, 123, doi: 10.3847/1538-3881/aabc4f

Batygin, K., Bodenheimer, P. H., & Laughlin, G. P. 2016, ApJ, 829, 114, doi: 10.3847/0004-637X/829/2/114

Beaugé, C., & Nesvorný, D. 2012, ApJ, 751, 119, doi: 10.1088/0004-637X/751/2/119

Bell, T. J., Dang, L., Cowan, N. B., et al. 2020, arXiv e-prints, arXiv:2010.00687. https://arxiv.org/abs/2010.00687

Bergmann, C., Jones, M. I., Zhao, J., et al. 2021, arXiv e-prints, arXiv:2102.08902. https://arxiv.org/abs/2102.08902

Blackman, R. T., Fischer, D. A., Jurgenson, C. A., et al. 2020, AJ, 159, 238, doi: 10.3847/1538-3881/ab811d

Blanco-Cuaresma, S. 2019, MNRAS, 486, 2075, doi: 10.1093/mnras/stz549

Blanco-Cuaresma, S., Soubiran, C., Heiter, U., & Jofré, P. 2014, A&A, 569, A111, doi: 10.1051/0004-6361/201423945

Böhm-Vitense, E. 2006, PASP, 118, 419, doi: 10.1086/499385

—. 2007, AJ, 133, 1903, doi: 10.1086/512124

Bolton, C. T. 1971, A&A, 14, 233

Borucki, W. J., Koch, D., Basri, G., et al. 2010, Science, 327, 977, doi: 10.1126/science.1185402

Bouchy, F., Hébrard, G., Udry, S., et al. 2009, A&A, 505, 853, doi: 10.1051/0004-6361/200912427

Bowler, B. P., Johnson, J. A., Marcy, G. W., et al. 2010, ApJ, 709, 396, doi: 10.1088/0004-637X/709/1/396

Brahm, R., Jordán, A., & Espinoza, N. 2017, PASP, 129, 034002, doi: 10.1088/1538-3873/aa5455

Brahm, R., Nielsen, L. D., Wittenmyer, R. A., et al. 2020, AJ, 160, 235, doi: 10.3847/1538-3881/abba3b

Brewer, J. M., Fischer, D. A., Blackman, R. T., et al. 2020, AJ, 160, 67, doi: 10.3847/1538-3881/ab99c9

Brown, T. M., Baliber, N., Bianco, F. B., et al. 2013a, Publications of the Astronomical Society of the Pacific, 125, 1031, doi: 10.1086/673168

—. 2013b, PASP, 125, 1031, doi: 10.1086/673168

Bryson, S., Kunimoto, M., Kopparapu, R. K., et al. 2021, AJ, 161, 36, doi: 10.3847/1538-3881/abc418

Buchhave, L. A., Bakos, G. Á., Hartman, J. D., et al. 2010, ApJ, 720, 1118, doi: 10.1088/0004-637X/720/2/1118

Buchhave, L. A., Latham, D. W., Johansen, A., et al. 2012, Nature, 486, 375, doi: 10.1038/nature11121

Buchhave, L. A., Bizzarro, M., Latham, D. W., et al. 2014, Nature, 509, 593, doi: 10.1038/nature13254

Butler, R. P., Marcy, G. W., Fischer, D. A., et al. 1999, ApJ, 526, 916, doi: 10.1086/308035

Butler, R. P., Marcy, G. W., Vogt, S. S., & Apps, K. 1998, PASP, 110, 1389, doi: 10.1086/316287

Cañas, C. I., Wang, S., Mahadevan, S., et al. 2019, ApJL, 870, L17, doi: 10.3847/2041-8213/aafa1e

Castelli, F., & Kurucz, R. L. 2003, in Modelling of Stellar Atmospheres, ed. N. Piskunov, W. W. Weiss, & D. F. Gray, Vol. 210, A20. https://arxiv.org/abs/astro-ph/0405087

Charbonneau, P. 1993, in Astronomical Society of the Pacific Conference Series, Vol. 44, IAU Colloq. 138: Peculiar versus Normal Phenomena in A-type and Related Stars, ed. M. M. Dworetsky, F. Castelli, & R. Faraggiana, 474

Chatterjee, S., Ford, E. B., Matsumura, S., & Rasio, F. A. 2008, ApJ, 686, 580, doi: 10.1086/590227

Choi, J., Dotter, A., Conroy, C., et al. 2016, The Astrophysical Journal, 823, 102

Claret, A. 2017, A&A, 600, A30, doi: 10.1051/0004-6361/201629705

Cochran, W. D., Hatzes, A. P., Butler, R. P., & Marcy, G. W. 1997, ApJ, 483, 457, doi: 10.1086/304245

Collier Cameron, A., Bruce, V. A., Miller, G. R. M., Triaud, A. H. M. J., & Queloz, D. 2010a, MNRAS, 403, 151, doi: 10.1111/j.1365-2966.2009.16131.x

Collier Cameron, A., Guenther, E., Smalley, B., et al. 2010b, MNRAS, 407, 507, doi: 10.1111/j.1365-2966.2010.16922.x

Collins, K. A., Kielkopf, J. F., Stassun, K. G., & Hessman, F. V. 2017, AJ, 153, 77, doi: 10.3847/1538-3881/153/2/77

Conti, P. S. 1970, PASP, 82, 781, doi: 10.1086/128965
Courcol, B., Bouchy, F., Pepe, F., et al. 2015, A&A, 581, A38, doi: 10.1051/0004-6361/201526329
Cowan, N. B., & Agol, E. 2011, ApJ, 729, 54, doi: 10.1088/0004-637X/729/1/54
Cumming, A., Marcy, G. W., & Butler, R. P. 1999, ApJ, 526, 890, doi: 10.1086/308020
Cutri, R. M., Skrutskie, M. F., van Dyk, S., et al. 2003, VizieR Online Data Catalog, II/246
—. 2013, VizieR Online Data Catalog, II/328
Davis, A. B., Wang, S., Jones, M., et al. 2020, AJ, 160, 229, doi: 10.3847/1538-3881/aba49d
Daylan, T., Günther, M. N., Mikal-Evans, T., et al. 2021, AJ, 161, 131
Djupvik, A. A., & Andersen, J. 2010, Astrophysics and Space Science Proceedings, 14, 211, doi: 10.1007/978-3-642-11250-8_21
Dorn, C., Harrison, J. H. D., Bonsor, A., & Hands, T. O. 2019, MNRAS, 484, 712, doi: 10.1093/mnras/sty3435
Dotter, A. 2016, The Astrophysical Journal Supplement Series, 222, 8
Eastman, J. 2017, EXOFASTv2: Generalized publication-quality exoplanet modeling code, Astrophysics Source Code Library. http://ascl.net/1710.003
Eastman, J., Gaudi, B. S., & Agol, E. 2013, PASP, 125, 83, doi: 10.1086/669497
Eastman, J. D., Rodriguez, J. E., Agol, E., et al. 2019, arXiv e-prints, arXiv:1907.09480. https://arxiv.org/abs/1907.09480
Endl, M., Cochran, W. D., Wittenmyer, R. A., & Boss, A. P. 2008, ApJ, 673, 1165, doi: 10.1086/524703
Figueras, F., Torra, J., & Jordi, C. 1991, A&AS, 87, 319
Fortney, J. J., Marley, M. S., & Barnes, J. W. 2007, ApJ, 659, 1661, doi: 10.1086/512120
Frandsen, S., & Lindberg, B. 1999, in Astrophysics with the NOT, ed. H. Karttunen & V. Piirola, 71
Fredslund Andersen, M., Handberg, R., Weiss, E., et al. 2019, PASP, 131, 045003, doi: 10.1088/1538-3873/aaff7c
Gaia Collaboration, Brown, A. G. A., Vallenari, A., et al. 2018a, A&A, 616, A1, doi: 10.1051/0004-6361/201833051
—. 2018b, A&A, 616, A1, doi: 10.1051/0004-6361/201833051
Gilbert, E. A., Barclay, T., Schlieder, J. E., et al. 2020, AJ, 160, 116, doi: 10.3847/1538-3881/aba4b2
Ginzburg, S., & Sari, R. 2015, ApJ, 803, 111, doi: 10.1088/0004-637X/803/2/111
Gray, R. O., & Corbally, C. J. 1994, AJ, 107, 742, doi: 10.1086/116893
Grundahl, F., Fredslund Andersen, M., Christensen-Dalsgaard, J., et al. 2017, ApJ, 836, 142, doi: 10.3847/1538-4357/836/1/142
Guenther, E. W., Barragán, O., Dai, F., et al. 2017, A&A, 608, A93, doi: 10.1051/0004-6361/201730885
Günther, M. N., & Daylan, T. 2019, Allesfitter: Flexible Star and Exoplanet Inference From Photometry and Radial Velocity, Astrophysics Source Code Library. http://ascl.net/1903.003
—. 2020, arXiv e-prints, arXiv:2003.14371. https://arxiv.org/abs/2003.14371
Günther, M. N., Pozuelos, F. J., Dittmann, J. A., et al. 2019, Nature Astronomy, 3, 1099, doi: 10.1038/s41550-019-0845-5
Gustafsson, B., Edvardsson, B., Eriksson, K., et al. 2008, A&A, 486, 951, doi: 10.1051/0004-6361:200809724
Hasegawa, Y., Yu, T. Y. M., & Hansen, B. M. S. 2019, A&A, 629, L1, doi: 10.1051/0004-6361/201936138
Heiter, U., Lind, K., Asplund, M., et al. 2015, PhyS, 90, 054010, doi: 10.1088/0031-8949/90/5/054010
Hellier, C., Anderson, D. R., Barkaoui, K., et al. 2019, MNRAS, 490, 1479, doi: 10.1093/mnras/stz2713
Henry, G. W., Marcy, G. W., Butler, R. P., & Vogt, S. S. 2000, ApJL, 529, L41, doi: 10.1086/312458
Hippke, M., David, T. J., Mulders, G. D., & Heller, R. 2019, AJ, 158, 143, doi: 10.3847/1538-3881/ab3984
Hirano, T., Narita, N., Sato, B., et al. 2011, PASJ, 63, L57, doi: 10.1093/pasj/63.6.L57
Hjorth, M., Albrecht, S., Hirano, T., et al. 2021, Proceedings of the National Academy of Science, 118, 2017418118, doi: 10.1073/pnas.2017418118
Hoeijmakers, H. J., Seidel, J. V., Pino, L., et al. 2020, A&A, 641, A123, doi: 10.1051/0004-6361/202038365
Høg, E., Fabricius, C., Makarov, V. V., et al. 2000, A&A, 355, L27
Horner, J., Kane, S. R., Marshall, J. P., et al. 2020, PASP, 132, 102001, doi: 10.1088/1538-3873/ab8eb9
Hsu, D. C., Ford, E. B., Ragozzine, D., & Ashby, K. 2019, AJ, 158, 109, doi: 10.3847/1538-3881/ab31ab
Huang, C. X., Burt, J., Vanderburg, A., et al. 2018, ApJL, 868, L39, doi: 10.3847/2041-8213/aaef91
Hunter, J. D. 2007, Computing In Science & Engineering, 9, 90, doi: 10.1109/MCSE.2007.55
Husser, T. O., Wende-von Berg, S., Dreizler, S., et al. 2013, A&A, 553, A6, doi: 10.1051/0004-6361/201219058
Ida, S., & Lin, D. N. C. 2005, ApJ, 626, 1045, doi: 10.1086/429953

Jenkins, J. M., Twicken, J. D., McCauliff, S., et al. 2016, in Society of Photo-Optical Instrumentation Engineers (SPIE) Conference Series, Vol. 9913, Proc. SPIE, 99133E, doi: 10.1117/12.2233418

Jensen, E. 2013, Tapir: A web interface for transit/eclipse observability, Astrophysics Source Code Library. http://ascl.net/1306.007

Johnson, J. A., Marcy, G. W., Fischer, D. A., et al. 2006, ApJ, 652, 1724, doi: 10.1086/508255

Johnson, M. C., Cochran, W. D., Albrecht, S., et al. 2014, ApJ, 790, 30, doi: 10.1088/0004-637X/790/1/30

Jones, H. R. A., Butler, R. P., Tinney, C. G., et al. 2006, MNRAS, 369, 249, doi: 10.1111/j.1365-2966.2006.10298.x

Jones, M. I., Jenkins, J. S., Brahm, R., et al. 2016, A&A, 590, A38, doi: 10.1051/0004-6361/201628067

Jones, M. I., Brahm, R., Espinoza, N., et al. 2019, A&A, 625, A16, doi: 10.1051/0004-6361/201834640

Jordán, A., Brahm, R., Espinoza, N., et al. 2020, AJ, 159, 145, doi: 10.3847/1538-3881/ab6f67

Jurgenson, C., Fischer, D., McCracken, T., et al. 2016, in Society of Photo-Optical Instrumentation Engineers (SPIE) Conference Series, Vol. 9908, Ground-based and Airborne Instrumentation for Astronomy VI, ed. C. J. Evans, L. Simard, & H. Takami, 99086T, doi: 10.1117/12.2233002

Kempton, E. M. R., Bean, J. L., Louie, D. R., et al. 2018, PASP, 130, 114401, doi: 10.1088/1538-3873/aadf6f

Komacek, T. D., Thorngren, D. P., Lopez, E. D., & Ginzburg, S. 2020, ApJ, 893, 36, doi: 10.3847/1538-4357/ab7eb4

Kovács, G., Zucker, S., & Mazeh, T. 2002, A&A, 391, 369, doi: 10.1051/0004-6361:20020802

Kozai, Y. 1962, AJ, 67, 591, doi: 10.1086/108790

Kurucz, R. L. 1993, SYNTHE spectrum synthesis programs and line data (None)

Levine, S. E., Bida, T. A., Chylek, T., et al. 2012, in Society of Photo-Optical Instrumentation Engineers (SPIE) Conference Series, Vol. 8444, Ground-based and Airborne Telescopes IV, ed. L. M. Stepp, R. Gilmozzi, & H. J. Hall, 844419, doi: 10.1117/12.926415

Li, D., Mustill, A. J., & Davies, M. B. 2019a, MNRAS, 488, 1366, doi: 10.1093/mnras/stz1794

Li, J., Tenenbaum, P., Twicken, J. D., et al. 2019b, PASP, 131, 024506, doi: 10.1088/1538-3873/aaf44d

Lidov, M. L. 1962, Planet. Space Sci., 9, 719, doi: 10.1016/0032-0633(62)90129-0

Lin, D. N. C., Bodenheimer, P., & Richardson, D. C. 1996, Nature, 380, 606, doi: 10.1038/380606a0

Louden, E. M., Winn, J. N., Petigura, E. A., et al. 2021, AJ, 161, 68, doi: 10.3847/1538-3881/abcebd

Luhn, J. K., Bastien, F. A., Wright, J. T., et al. 2019, AJ, 157, 149, doi: 10.3847/1538-3881/aaf5d0

Lund, M. B., Rodriguez, J. E., Zhou, G., et al. 2017, AJ, 154, 194, doi: 10.3847/1538-3881/aa8f95

Martínez, R. R., Gaudi, B. S., Rodriguez, J. E., et al. 2020, AJ, 160, 111, doi: 10.3847/1538-3881/ab9f2d

Mayor, M., & Queloz, D. 1995, Nature, 378, 355, doi: 10.1038/378355a0

McCully, C., Volgenau, N. H., Harbeck, D.-R., et al. 2018, in Society of Photo-Optical Instrumentation Engineers (SPIE) Conference Series, Vol. 10707, Proc. SPIE, 107070K, doi: 10.1117/12.2314340

McLaughlin, D. B. 1924, ApJ, 60, 22, doi: 10.1086/142826

Mészáros, S., Allende Prieto, C., Edvardsson, B., et al. 2012, AJ, 144, 120, doi: 10.1088/0004-6256/144/4/120

Michaud, G., Tarasick, D., Charland, Y., & Pelletier, C. 1983, ApJ, 269, 239, doi: 10.1086/161034

Millholland, S., Wang, S., & Laughlin, G. 2016, ApJL, 823, L7, doi: 10.3847/2041-8205/823/1/L7

—. 2017, ApJL, 849, L33, doi: 10.3847/2041-8213/aa9714

Mills, S. M., Howard, A. W., Weiss, L. M., et al. 2019, AJ, 157, 145, doi: 10.3847/1538-3881/ab0899

Morris, R. L., Twicken, J. D., Smith, J. C., et al. 2020, Kepler Data Processing Handbook: Photometric Analysis, Kepler Science Document KSCI-19081-003

Naef, D., Latham, D. W., Mayor, M., et al. 2001, A&A, 375, L27, doi: 10.1051/0004-6361:20010853

Nagasawa, M., Ida, S., & Bessho, T. 2008, ApJ, 678, 498, doi: 10.1086/529369

Narita, N., Fukui, A., Kusakabe, N., et al. 2019, Journal of Astronomical Telescopes, Instruments, and Systems, 5, 015001, doi: 10.1117/1.JATIS.5.1.015001

Newton, E. R., Mann, A. W., Tofflemire, B. M., et al. 2019, ApJL, 880, L17, doi: 10.3847/2041-8213/ab2988

Parmentier, V., & Crossfield, I. J. M. 2018, Exoplanet Phase Curves: Observations and Theory (Springer International Publishing), 116, doi: 10.1007/978-3-319-55333-7_116

Parmentier, V., Line, M. R., Bean, J. L., et al. 2018, A&A, 617, A110, doi: 10.1051/0004-6361/201833059

Parviainen, H., Tingley, B., Deeg, H. J., et al. 2019, A&A, 630, A89, doi: 10.1051/0004-6361/201935709

Paxton, B., Bildsten, L., Dotter, A., et al. 2011, The Astrophysical Journal Supplement Series, 192, 3

Paxton, B., Cantiello, M., Arras, P., et al. 2013, The Astrophysical Journal Supplement Series, 208, 4

Paxton, B., Marchant, P., Schwab, J., et al. 2015, The Astrophysical Journal Supplement Series, 220, 15

Paxton, B., Schwab, J., Bauer, E., et al. 2018, The Astrophysical Journal Supplement Series, 234, 34

Paxton, B., Smolec, R., Schwab, J., et al. 2019, The Astrophysical Journal Supplement Series, 243, 10

Pepe, F., Mayor, M., Queloz, D., et al. 2004, A&A, 423, 385, doi: 10.1051/0004-6361:20040389

Perruchot, S., Kohler, D., Bouchy, F., et al. 2008, in Society of Photo-Optical Instrumentation Engineers (SPIE) Conference Series, Vol. 7014, Ground-based and Airborne Instrumentation for Astronomy II, ed. I. S. McLean & M. M. Casali, 70140J, doi: 10.1117/12.787379

Perruchot, S., Bouchy, F., Chazelas, B., et al. 2011, in Society of Photo-Optical Instrumentation Engineers (SPIE) Conference Series, Vol. 8151, Techniques and Instrumentation for Detection of Exoplanets V, ed. S. Shaklan, 815115, doi: 10.1117/12.892466

Perryman, M. A. C., Brown, A. G. A., Lebreton, Y., et al. 1998, A&A, 331, 81. https://arxiv.org/abs/astro-ph/9707253

Petersburg, R. R., Ong, J. M. J., Zhao, L. L., et al. 2020, AJ, 159, 187, doi: 10.3847/1538-3881/ab7e31

Piskunov, N. E., Kupka, F., Ryabchikova, T. A., Weiss, W. W., & Jeffery, C. S. 1995, A&AS, 112, 525

Plavchan, P., Barclay, T., Gagné, J., et al. 2020, Nature, 582, 497, doi: 10.1038/s41586-020-2400-z

Preston, G. W. 1974, ARA&A, 12, 257, doi: 10.1146/annurev.aa.12.090174.001353

Reffert, S., Bergmann, C., Quirrenbach, A., Trifonov, T., & Künstler, A. 2015a, A&A, 574, A116, doi: 10.1051/0004-6361/201322360

—. 2015b, A&A, 574, A116, doi: 10.1051/0004-6361/201322360

Renson, P., Gerbaldi, M., & Catalano, F. A. 1991, A&AS, 89, 429

Ricker, G. R., Winn, J. N., Vanderspek, R., et al. 2015, Journal of Astronomical Telescopes, Instruments, and Systems, 1, 014003, doi: 10.1117/1.JATIS.1.1.014003

Ritter, A., Hyde, E. A., & Parker, Q. A. 2014, PASP, 126, 170, doi: 10.1086/675407

Rodríguez Martínez, R., Gaudi, B. S., Rodriguez, J. E., et al. 2020, AJ, 160, 111, doi: 10.3847/1538-3881/ab9f2d

Rogers, L. A. 2015, ApJ, 801, 41, doi: 10.1088/0004-637X/801/1/41

Rossiter, R. A. 1924, ApJ, 60, 15, doi: 10.1086/142825

Ryabchikova, T., Piskunov, N., Kurucz, R. L., et al. 2015, PhyS, 90, 054005, doi: 10.1088/0031-8949/90/5/054005

Saffe, C., Miquelarena, P., Alacoria, J., et al. 2020, A&A, 641, A145, doi: 10.1051/0004-6361/202038843

—. 2021, arXiv e-prints, arXiv:2101.04416. https://arxiv.org/abs/2101.04416

Schlafly, E. F., & Finkbeiner, D. P. 2011, ApJ, 737, 103, doi: 10.1088/0004-637X/737/2/103

Shporer, A. 2017, PASP, 129, 072001, doi: 10.1088/1538-3873/aa7112

Shporer, A., Wong, I., Huang, C. X., et al. 2019, AJ, 157, 178, doi: 10.3847/1538-3881/ab0f96

Siverd, R. J., Collins, K. A., Zhou, G., et al. 2018a, AJ, 155, 35, doi: 10.3847/1538-3881/aa9e4d

Siverd, R. J., Brown, T. M., Barnes, S., et al. 2018b, in Society of Photo-Optical Instrumentation Engineers (SPIE) Conference Series, Vol. 10702, Ground-based and Airborne Instrumentation for Astronomy VII, ed. C. J. Evans, L. Simard, & H. Takami, 107026C, doi: 10.1117/12.2312800

—. 2018c, AJ, 155, 35, doi: 10.3847/1538-3881/aa9e4d

Smith, J. C., Stumpe, M. C., Van Cleve, J. E., et al. 2012, PASP, 124, 1000, doi: 10.1086/667697

Sneden, C. 1973, ApJ, 184, 839, doi: 10.1086/152374

Sozzetti, A., Torres, G., Charbonneau, D., et al. 2007, ApJ, 664, 1190, doi: 10.1086/519214

Sozzetti, A., Damasso, M., Bonomo, A. S., et al. 2021, arXiv e-prints, arXiv:2101.12300. https://arxiv.org/abs/2101.12300

Stassun, K. G., & Torres, G. 2018, ApJ, 862, 61, doi: 10.3847/1538-4357/aacafc

Stassun, K. G., Oelkers, R. J., Paegert, M., et al. 2019, AJ, 158, 138, doi: 10.3847/1538-3881/ab3467

Stumpe, M. C., Smith, J. C., Catanzarite, J. H., et al. 2014, PASP, 126, 100, doi: 10.1086/674989

Stumpe, M. C., Smith, J. C., Van Cleve, J. E., et al. 2012, PASP, 124, 985, doi: 10.1086/667698

Talens, G. J. J., Spronck, J. F. P., Lesage, A. L., et al. 2017, A&A, 601, A11, doi: 10.1051/0004-6361/201630319

Tanaka, H., Takeuchi, T., & Ward, W. R. 2002, ApJ, 565, 1257, doi: 10.1086/324713

Telting, J. H., Avila, G., Buchhave, L., et al. 2014, Astronomische Nachrichten, 335, 41, doi: 10.1002/asna.201312007

Teske, J., Díaz, M. R., Luque, R., et al. 2020, AJ, 160, 96, doi: 10.3847/1538-3881/ab9f95

Thorngren, D., & Fortney, J. 2018, The Astronomical Journal, 155, 214

Tinetti, G., Drossart, P., Eccleston, P., et al. 2018, Experimental Astronomy, 46, 135, doi: 10.1007/s10686-018-9598-x

Tinney, C. G., Butler, R. P., Marcy, G. W., et al. 2001a, ApJ, 551, 507, doi: 10.1086/320097

—. 2001b, ApJ, 551, 507, doi: 10.1086/320097

Torres, G., Fischer, D. A., Sozzetti, A., et al. 2012, ApJ, 757, 161, doi: 10.1088/0004-637X/757/2/161

Triaud, A. H. M. J., Collier Cameron, A., Queloz, D., et al. 2010, A&A, 524, A25, doi: 10.1051/0004-6361/201014525

Trifonov, T., Reffert, S., Tan, X., Lee, M. H., & Quirrenbach, A. 2014, A&A, 568, A64, doi: 10.1051/0004-6361/201322885

Tsantaki, M., Andreasen, D. T., Teixeira, G. D. C., et al. 2018, MNRAS, 473, 5066, doi: 10.1093/mnras/stx2564

Twicken, J. D., Clarke, B. D., Bryson, S. T., et al. 2010, in Society of Photo-Optical Instrumentation Engineers (SPIE) Conference Series, Vol. 7740, Proc. SPIE, 774023, doi: 10.1117/12.856790

Twicken, J. D., Catanzarite, J. H., Clarke, B. D., et al. 2018, PASP, 130, 064502, doi: 10.1088/1538-3873/aab694

Valenti, J. A., & Fischer, D. A. 2005, ApJS, 159, 141, doi: 10.1086/430500

Vogt, S. S., Wittenmyer, R. A., Butler, R. P., et al. 2010, ApJ, 708, 1366, doi: 10.1088/0004-637X/708/2/1366

von Essen, C., Mallonn, M., Borre, C. C., et al. 2020, A&A, 639, A34, doi: 10.1051/0004-6361/202037905

Wakeford, H. R., Visscher, C., Lewis, N. K., et al. 2017, MNRAS, 464, 4247, doi: 10.1093/mnras/stw2639

Wang, S., Jones, M., Shporer, A., et al. 2019, AJ, 157, 51, doi: 10.3847/1538-3881/aaf1b7

Ward, W. R. 1997, Icarus, 126, 261, doi: 10.1006/icar.1996.5647

Weiss, L. M., Fabrycky, D. C., Agol, E., et al. 2020, AJ, 159, 242, doi: 10.3847/1538-3881/ab88ca

Winn, J. N., Fabrycky, D., Albrecht, S., & Johnson, J. A. 2010, ApJL, 718, L145, doi: 10.1088/2041-8205/718/2/L145

Winn, J. N., Johnson, J. A., Albrecht, S., et al. 2009, ApJL, 703, L99, doi: 10.1088/0004-637X/703/2/L99

Winn, J. N., Holman, M. J., Torres, G., et al. 2008, ApJ, 683, 1076, doi: 10.1086/589737

Wittenmyer, R. A., Clark, J. T., Zhao, J., et al. 2019, MNRAS, 484, 5859, doi: 10.1093/mnras/stz290

Wittenmyer, R. A., Jones, M. I., Horner, J., et al. 2017, AJ, 154, 274, doi: 10.3847/1538-3881/aa9894

Wittenmyer, R. A., Butler, R. P., Horner, J., et al. 2020, MNRAS, 491, 5248, doi: 10.1093/mnras/stz3378

Wong, I., Benneke, B., Shporer, A., et al. 2020a, AJ, 159, 104, doi: 10.3847/1538-3881/ab6d6e

Wong, I., Shporer, A., Kitzmann, D., et al. 2020b, AJ, 160, 88, doi: 10.3847/1538-3881/aba2cb

Wong, I., Shporer, A., Daylan, T., et al. 2020c, AJ, 160, 155, doi: 10.3847/1538-3881/ababad

Wright, J. T., Marcy, G. W., Butler, R. P., et al. 2008, ApJL, 683, L63, doi: 10.1086/587461

Xiang, M.-S., Rix, H.-W., Ting, Y.-S., et al. 2020, ApJ, 898, 28, doi: 10.3847/1538-4357/ab99a5

Yi, S., Demarque, P., Kim, Y.-C., et al. 2001, ApJS, 136, 417, doi: 10.1086/321795

Zhou, G., Latham, D. W., Bieryla, A., et al. 2016a, MNRAS, 460, 3376, doi: 10.1093/mnras/stw1107

Zhou, G., Rodriguez, J. E., Collins, K. A., et al. 2016b, AJ, 152, 136, doi: 10.3847/0004-6256/152/5/136

—. 2016c, AJ, 152, 136, doi: 10.3847/0004-6256/152/5/136

Zinnecker, H., & Yorke, H. W. 2007, ARA&A, 45, 481, doi: 10.1146/annurev.astro.44.051905.092549

Table 4. A summary of the ground-based transit follow-up observations taken of TOI-1431.

Telescope	Camera	Filter	UT Date	Coverage	Precision (ppt)	Joint Fit	Comments
CDK14	STXL-6303E	z'	2019-12-24	Full	2.62	No	Minimal systematics
CDK14	STXL-6303E	g'	2019-12-24	Full	2.32	No	Minimal systematics
TCS	MuSCAT2	g'	2020-05-16	Full	0.93	Yes	Minimal systematics
TCS	MuSCAT2	r'	2020-05-16	Full	0.97	Yes	Minimal systematics
TCS	MuSCAT2	i'	2020-05-16	Full	0.94	Yes	Minimal systematics
TCS	MuSCAT2	z_s	2020-05-16	Full	1.01	Yes	Minimal systematics
TCS	MuSCAT2	g'	2020-05-23	Full	1.23	No	Limited pre-ingress data and systematics
TCS	MuSCAT2	r'	2020-05-23	Full	1.07	No	Limited pre-ingress data and systematics
TCS	MuSCAT2	i'	2020-05-23	Full	1.08	No	Limited pre-ingress data and systematics
TCS	MuSCAT2	z_s	2020-05-23	Full	1.09	No	Limited pre-ingress data and systematics
AUKR	ALTA U47	z'	2020-06-16	Full	3.09	No	Some systematics
LCOGT-McD	Sinistro	PANSTARRS Y	2020-07-13	Ingress	0.48	No	Ingress only
SCT	ST7XME	*TESS* band	2020-08-08	Full	1.49	No	Minimal systematics
ULMT	STX 16803	i'	2020-09-20	Full	3.41	No	Significant systematics
ULMT	STX 16803	i'	2020-09-28	Full	0.73	No	Significant systematics
LCOGT-McD	Sinistro	PANSTARRS Y	2020-10-14	Full	1.18	Yes	Minimal systematics

APPENDIX

Table 5. Radial Velocity Measurements

Date[a] BJD - 2400000	RV[b] (m s^{-1})	$\sigma_{\rm RV}$ (m s^{-1})	Instrument
58805.564199	-25696.6	14.5	ELP
58806.565002	-25761.0	15.3	ELP
58807.566340	-25346.6	13.3	ELP
58808.570467	-25830.7	29.9	ELP
58814.663425	-25557.9	26.2	ELP
58815.307593	9.2	14.2	FIES
58818.618086	-25457.5	18.0	ELP
58836.224800	-25039.0	7.0	SOPHIE
58838.252200	-25441.0	7.0	SOPHIE
58840.399100	-25532.0	45.0	SOPHIE
58841.235500	-25222.0	7.0	SOPHIE
58841.352100	-25152.0	6.0	SOPHIE
58859.232100	-25528.0	7.0	SOPHIE
58860.267700	-24987.0	6.0	SOPHIE
58861.259600	-25374.0	6.0	SOPHIE
58914.768952	-25465.4	53.1	SONG
58919.763375	-25434.9	81.7	SONG
58921.764647	-24969.6	74.1	SONG
58942.562272	-25283.8	19.2	TLV
58943.567282	-25788.4	15.4	TLV
58948.564452	-25514.9	16.4	TLV
58952.584719	-25528.9	16.3	TLV
58955.532830	-25299.7	28.7	TLV
58956.668739	-25303.1	139.4	SONG

Table 5 *continued*

Table 5 *(continued)*

Date[a] BJD - 2400000	RV[b] (m s^{-1})	$\sigma_{\rm RV}$ (m s^{-1})	Instrument
58961.645589	-25067.3	56.1	SONG
58965.721756	-25219.0	44.1	SONG
58980.495174	-25900.9	19.9	TLV
58982.464359	-25256.1	27.5	TLV
58983.637401	-25477.9	64.2	SONG
58987.442635	-25265.9	22.1	TLV
58988.470752	-25659.4	27.9	TLV
58988.619270	-25374.0	26.6	SONG
58989.466532	-25588.9	42.2	TLV
58990.449283	-25278.6	20.1	TLV
58990.567802	-24.1	7.9	FIES
58991.456242	-25896.5	26.1	TLV
58991.562807	-581.4	15.6	FIES
58991.594498	-565.9	12.9	FIES
58991.642527	-25435.4	18.0	SONG
58991.698593	-565.4	11.0	FIES
58992.606914	-69.5	12.5	FIES
58992.615274	-75.2	18.9	FIES
58993.658735	-318.3	11.6	FIES
58993.662679	-339.5	15.6	FIES
58993.666687	-314.2	14.1	FIES
58993.670878	-329.4	18.3	FIES
58993.674862	-315.8	11.2	FIES
58993.678937	-333.8	13.4	FIES
58993.686045	-334.8	9.8	FIES
58993.690092	-329.0	13.9	FIES
58993.694137	-337.2	13.8	FIES

Table 5 *continued*

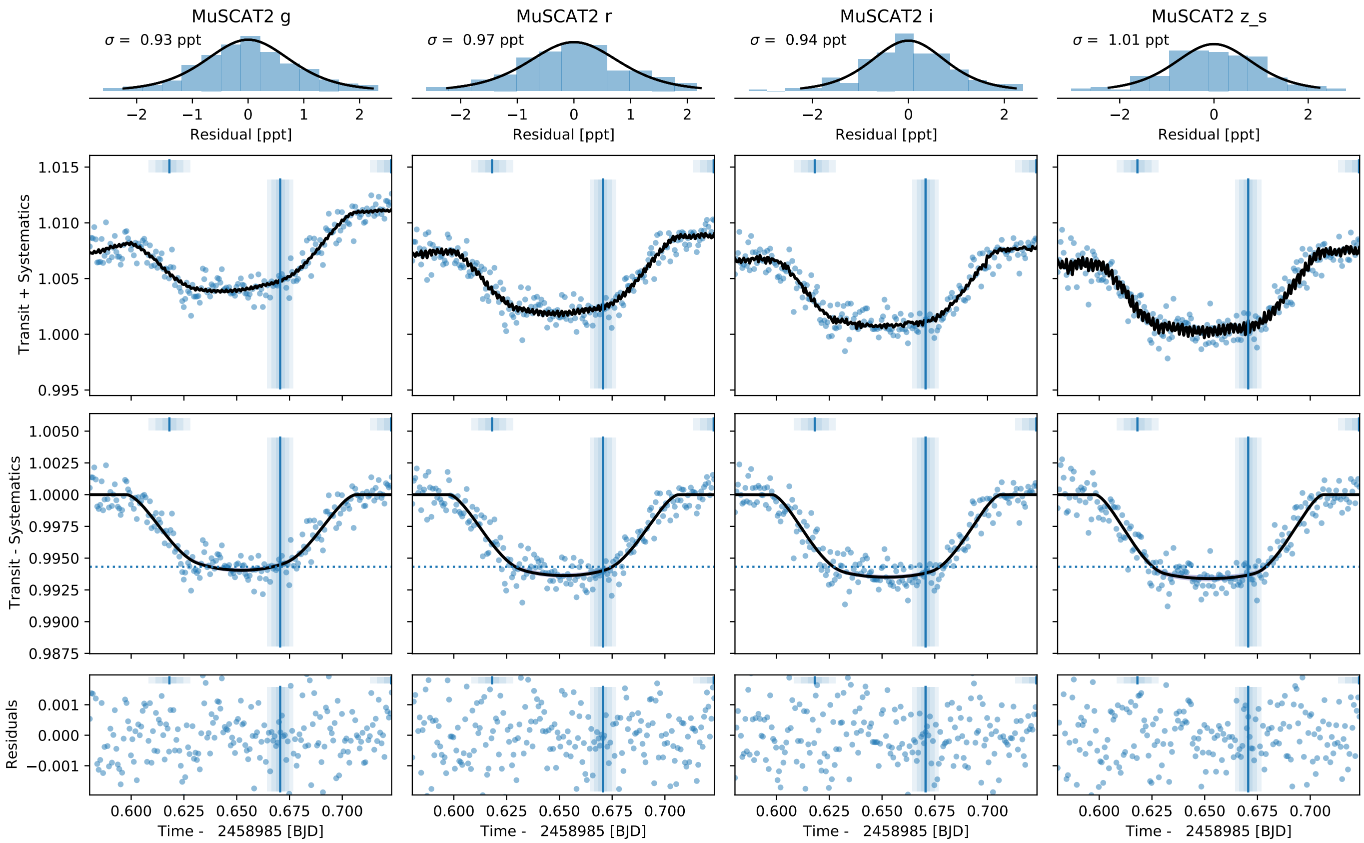

Figure 17. An observed transit on 16 May 2020 by MuSCAT2 using simultaneous multi-color photometry in g', r', i', and z_s bands. The top panel shows the distribution of residuals to the fit of the light curve in each band. The second panel from the top shows the fit to the transit plus systematics. The third panel shows the fit to the transit with the systematics removed. The three blue vertical bars in the second, third, and fourth panels represent the predicted ingress, mid-transit, and egress times along with their 1σ uncertainties based on the ephemeris used at the time. The horizontal dotted blue lines in the third panel show the predicted transit depth. The bottom panel shows the resulting residuals to the fit of the light curves.

Table 5 *(continued)*

Date[a]	RV[b]	$\sigma_{\rm RV}$	Instrument
BJD - 2400000	(m s^{-1})	(m s^{-1})	
58993.698146	-345.5	9.7	FIES
58994.571980	-500.4	9.3	FIES
58994.621049	-471.6	8.0	FIES
58994.704411	-429.4	11.7	FIES
58995.443468	-25324.0	28.7	TLV
58995.570851	15.5	11.5	FIES
58995.620876	13.7	7.2	FIES
58995.703476	0.0	11.9	FIES
58996.502720	-25732.7	26.1	TLV
58997.422153	-25702.1	38.1	TLV
58998.422132	-25287.5	23.5	TLV
58999.424288	-25873.9	19.0	TLV
58999.624293	-25458.0	76.4	SONG
59001.471298	-25606.2	20.1	TLV
59001.641856	-25224.1	28.8	SONG
59002.428683	-25802.8	21.2	TLV
59002.787631	-55.3	2.5	EXPRES

Table 5 *continued*

Table 5 *(continued)*

Date[a]	RV[b]	$\sigma_{\rm RV}$	Instrument
BJD - 2400000	(m s^{-1})	(m s^{-1})	
59003.954076	167.7	1.8	EXPRES
59004.452546	-25721.2	16.9	TLV
59004.602433	-25375.3	24.6	SONG
59004.953876	-279.8	2.0	EXPRES
59005.450710	-25560.8	18.8	TLV
59006.382260	-25320.8	19.6	TLV
59007.421885	-25873.3	17.2	TLV
59007.604415	-25444.7	39.9	SONG
59008.456417	-25235.3	34.6	TLV
59009.487869	-25570.9	18.7	TLV
59009.566599	-25187.8	24.2	SONG
59010.502769	-25751.8	19.5	TLV
59010.624528	-25295.0	24.9	SONG
59012.426456	-25777.6	16.5	TLV
59012.640398	-25419.6	29.3	SONG
59012.955625	-271.6	1.9	EXPRES
59018.520808	-447.3	17.6	FIES

Table 5 *continued*

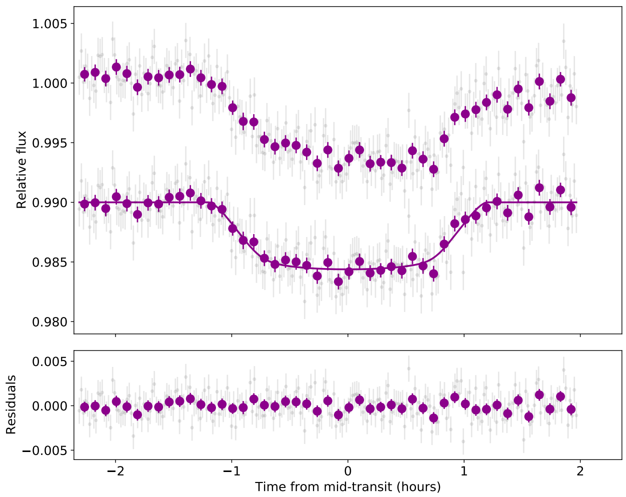

Figure 18. A transit of TOI-1431 b observed on 14 October 2020 by the LCOGT 1 m network in PANSTARRS Y-band. The top panel shows the undetrended and detrended light curves. The detrended light curve is shifted by -10 ppt on the y-axis for clarity. The solid line shows the best fit transit model. The bottom panel shows the model residuals. The individually fitted transit depth is $5.5^{+0.4}_{-0.3}$ ppt.

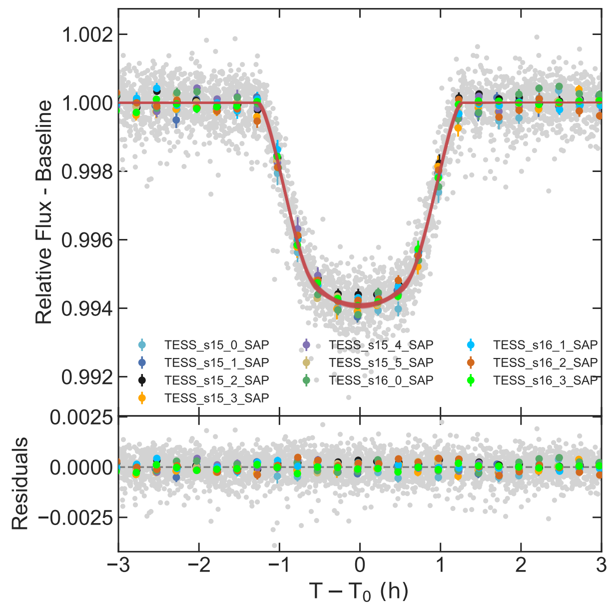

Figure 19. Phase-folded and detrended light curve of TOI-1431 from the simultaneous hybrid cubic spline detrending model using the SAP data. The colored points represent the individual phased light curve segments across Sectors 15 and 16 that have been binned at a cadence of 15 m. The red solid lines are 20 light curve models drawn from the posteriors of the Nested Sampling analysis in `Allesfitter`.

Table 5 *(continued)*

Date[a]	RV[b]	$\sigma_{\rm RV}$	Instrument
BJD - 2400000	(m s^{-1})	(m s^{-1})	
59018.597262	-406.4	15.7	FIES
59018.693433	-330.5	8.5	FIES
59019.513133	34.7	8.4	FIES
59019.594250	2.8	7.5	FIES
59019.694408	-25.8	9.3	FIES
59020.514030	-516.7	10.5	FIES
59020.590422	-546.9	9.0	FIES
59020.688977	-552.9	12.6	FIES
59023.610494	-25418.5	21.3	SONG
59027.569361	-24874.0	24.4	SONG
59029.510059	-25065.6	20.3	SONG
59033.957319	-287.7	2.2	EXPRES
59059.915400	-36.2	2.1	EXPRES
59059.919605	-44.0	2.0	EXPRES
59059.923762	-38.9	2.0	EXPRES
59059.927997	-45.9	2.2	EXPRES
59059.932407	-51.7	2.2	EXPRES
59059.936606	-50.3	2.3	EXPRES
59059.940835	-50.7	2.2	EXPRES
59059.945055	-58.2	2.1	EXPRES
59059.949247	-59.5	1.9	EXPRES
59059.953490	-62.4	2.3	EXPRES

[a] The dates for each observation are reported as BJD at the UTC time at the midpoint of the exposure.

[b] FIES and EXPRES radial velocities are given at an arbitrary zero point.

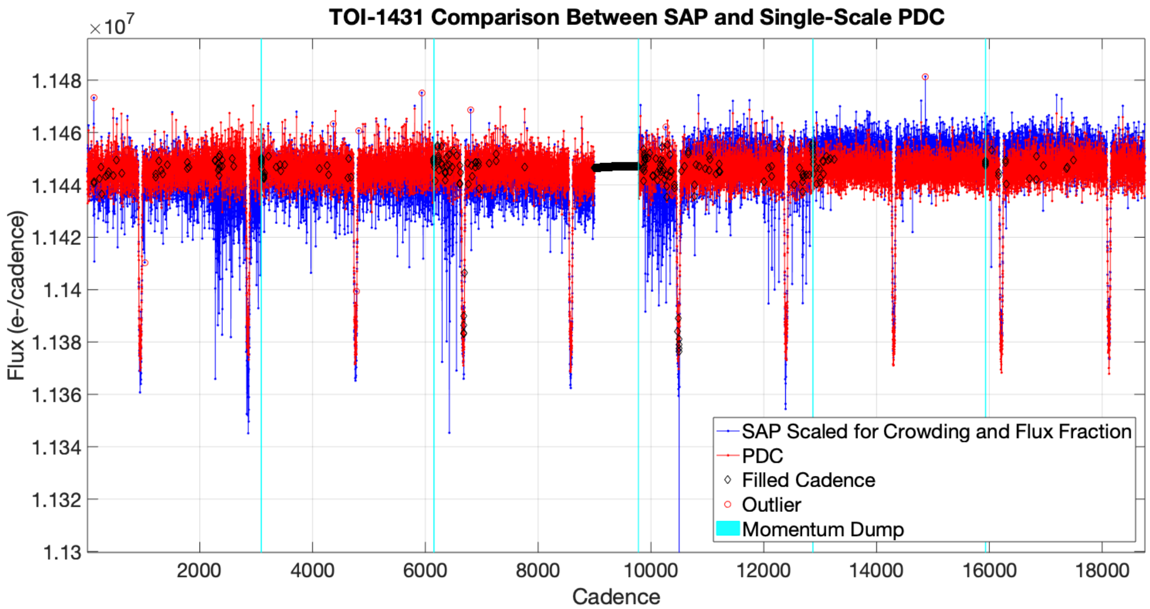

Figure 20. *TESS* Sector 15 photometry of TOI-1431 from the SAP (blue points) and single-scale MAP PDC (red points) light curves. The SAP light curve shows 'whisker'-like flux dips that are caused by brief spacecraft pointing excursions, some of which overlap with the transit events. The correction applied to the single-scale MAP PDC light curve from the use of the Co-trending Basis Vectors has removed these features.

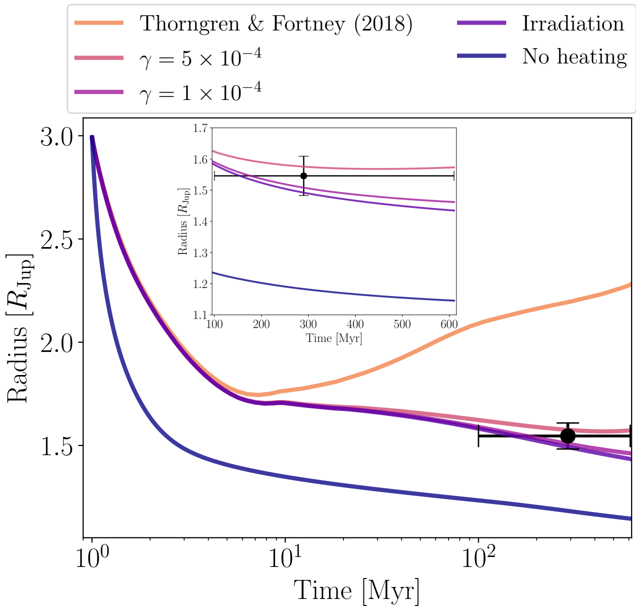

Figure 21. Radius evolution of TOI-1431b for various assumptions about the presence of irradiation and deep deposited heating. The curve labeled Thorngren & Fortney (2018) includes irradiation and applies deposited heating in the deep interior with a strength that varies with equilibrium temperature, as in Equation (34) of Thorngren & Fortney (2018). The models labeled $\gamma = 5\times10^{-4}$ and $\gamma = 1\times10^{-4}$ respectively assume that 0.05% and 0.01% of the incident stellar power is converted to heat deposited deep in the planetary interior and include irradiation. The model labeled "irradiation" considers only irradiation with no deposited heating, and the model labeled "no heating" does not include irradiation or deposited heating. Evolution models are conducted with `MESA` (Paxton et al. 2011, 2013, 2015, 2018, 2019) using the model setup described in Komacek et al. (2020) and stellar evolution tracks from Choi et al. (2016) and Dotter (2016). The present-day radius of TOI-1431b can be fit by planetary evolution models including only irradiation slowing cooling, but a small amount of deep deposited heating corresponding to $\lesssim 0.07\%$ of the incident stellar power converted to heat is allowed.

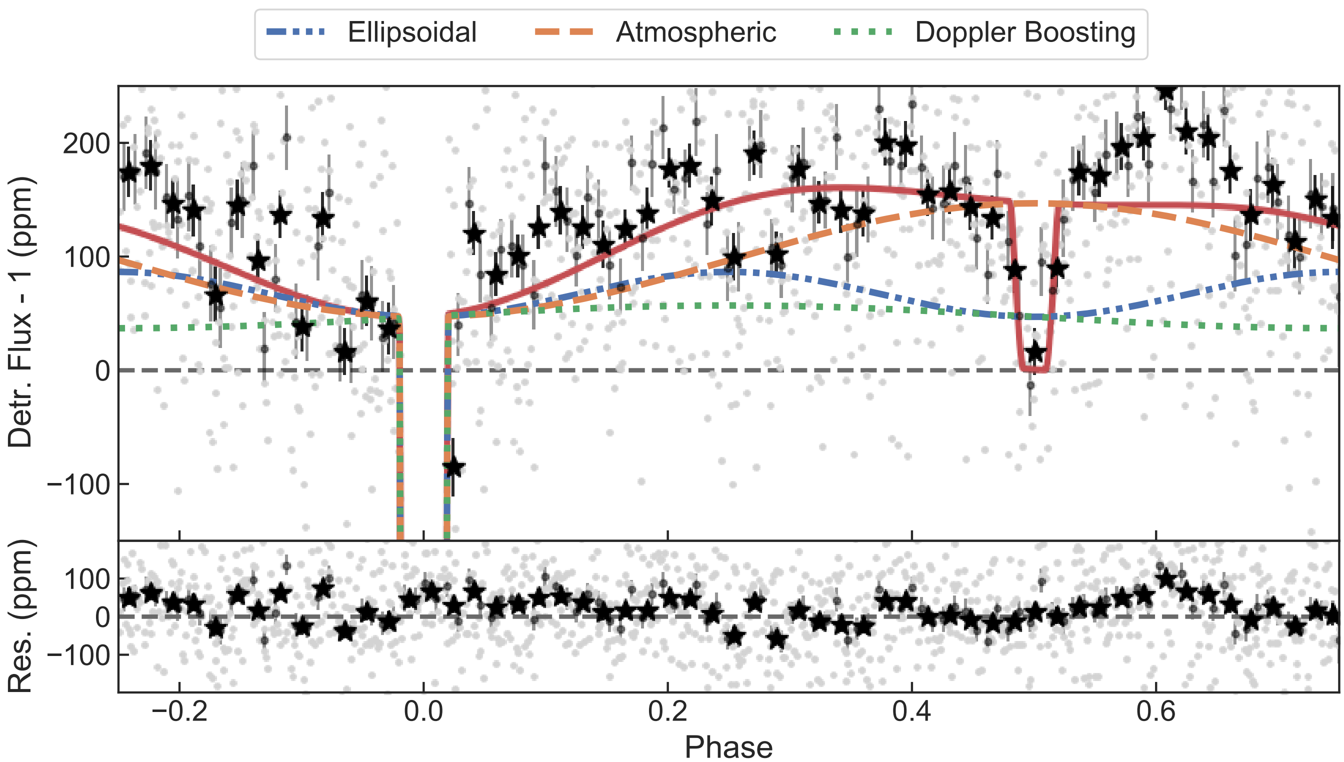

Figure 22. The phase-folded *TESS* SAP light curve for TOI-1431 b, zoomed in to show the phase curve and secondary eclipse, similar to Figure 11.